RESEARCH ACTIVITIES

Materials Molecular Science

Extensive development of new molecules, molecular systems and their higher-order assemblies is being conducted in the four divisions and in the research center for molecular scale nanoscience. Their electronic, optical and magnetic properties as well as reactivities and catalytic activities are being examined in an attempt to discover new phenomena and useful functions.

Graphene-Walled Alveolate Carbon & Structures and Functions of Metal–Carbon Nano-Systems Made from Metal-Acetylides

Department of Materials Molecular Science
Division of Electronic Structure

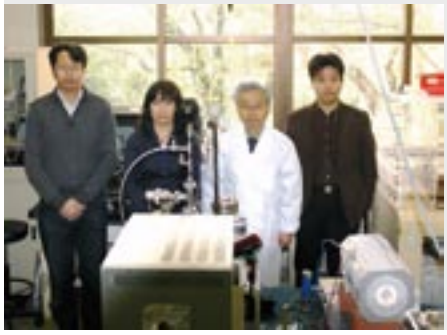

NISHI, Nobuyuki	Professor
JUDAI, Ken	Assistant Professor
NISHIJO, Junichi	Assistant Professor
USUI, Chika	Technical Fellow & Secretary

Metal acetylides or metal ethynyl molecules are made of the M^+–C^- ionic bonds. However, the ionic states of the acetylides are essentially metastable resulting in the segregation into metal-carbon or metal-organic polymer nanophases. Following to the invention of graphene-singlewalled Mesoporous Carbon Nano Dendrides (MCND) by evaporating silver from dendroid silver acetylide crystals, we have invented Graphene-multiwalled Alveolate Carbon (GAC), this time, and also 3D nanonets with GAC. These highly electron-conductive materials can be used for the electrodes of various next generation batteries.

1. Invention of Graphene-Multiwalled Alveolate Carbon for Novel Battery Electrodes

As demonstrated by the invention of graphene-walled Mesoporous Carbon Nano-Dendrites (MCND), metal- acetylides are well suited for generating nanostructured conductive materials. In contrast to silver acetylide, copper acetylide or methylethynyl copper normally produces wire-type crystals. Copper methylacetylide ($Cu–C{\equiv}C–CH_3$) also produces wire type crystals bigger and longer than those of copper acetylide. Following to the thermal activation at 230 °C under hydrogen atomosphere, the wire crystals filled in a 300 mL beaker suddenly exhibit the violent segregation reaction producing copper nanocrystals in carbon and a gas mixture of methane and ethylene. A part of copper nanoparticles is removed by the treatment with nitric acid and the residual copper particles are removed at a temperature higher than 1150 °C. The density of the remaining carbon material is 2.07 g/cm^3 that is 4.2% smaller than that of graphite (2.16 g/cm^3). Thermogravimetric Analysis showed a burning temperature as high as 682 °C: A little higher than that of MCND. The small angle X-ray scattering (SAXS) studies suggest that there are three types of the pores; the main part (69% in volume) has empty cores (an average size of 6 nm) surrounded with the shells of 0.83 nm thickness on average, the second one has nearly the same core radii but much thicker shells (17 nm av.), and the third one has

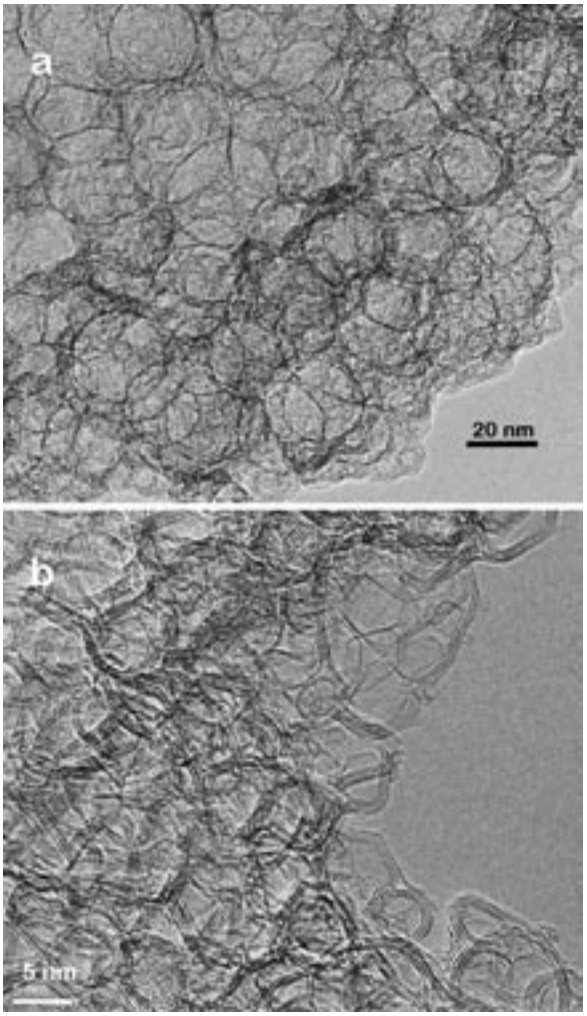

Figure 1. TEM images of a plate-type GAC treated at 1000 °C(**a**), and 1400 °C(**b**).

an average pore size of 40 nm: Each of them is located in the edge area of plate type alveolates, branch-type alveolate rods, and in the middle of big plates, respectively. TEM images of the carbon are shown in Figure 1. Figures 1-a and 1-b show the main component of the plate-type GAC, and the TEM image of the second component showed graphene-multiwalled rod-like alveolate carbon. According to these morphology and various properties, we call this carbon "Graphene-multiwalled Alveolate Carbon (GAC)."

The escape pathways of copper allow other atoms or molecules to be stored in the pores. Thus we have succeeded to store Sn and Si nanocrystals in the pores. Lithium ion batteries with these materials as negative electrodes have exhibited electric capacities as high as 1200–1400 mAh/cm^3 and almost flat charge/discharge cycle performance.

2. In Situ Preparation and Catalytic Activation Method for Copper Nano-Particles from Acetylide Molecules

Metallic surface is too reactive to keep its original structure under usual atmosphere. In order to avoid oxidation and inactivation, we propose a facile preparation method for catalysts of metal nano-particles in situ. Copper acetylide (C_2Cu_2) molecules and copper methyl-acetylide ($CuCC–CH_3$) molecules can be used as precursors of copper nano-particles. Figure 2 shows a High Resolution (HR)TEM image of which the nano-particle, atomically resolved lattice pattern was clearly observed. The space fringes detected in the HRTEM image are well matched with the d value (0.208 nm) of copper. The Cu nano-particle was covered with amorphous parts. The amorphous carbon layers can function as protection group for oxidation. Actually the metallic copper lattice could be observed even if the TEM specimen was exposed to air during transfer into the TEM apparatus. This means that the outer amorphous carbon could protect the reactive copper nano-particle from oxidizing by air.

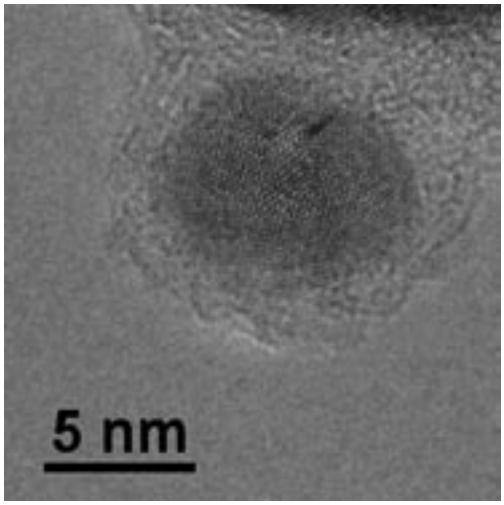

Figure 2. High-resolution transmission electron microscopic (HRTEM) image of annealed $CuCC–CH_3$ acetylide molecules.

3. Strong Intermolecular Interaction *via* Acetylide Ligands

Transition metal acetylide complex is the isoelectronic carbon analogue of a nitrile complex that is one of the representative building blocks of magnetic materials. In the previous work, we succeeded in constructing the first transition metal acetylide based magnets. However, in those cases, the acetylide ligand itself plays only a subsidiary role in the intermolecular spin–spin interactions because the ligand is placed too far from adjacent molecules to interact. That is, the appropriateness of an acetylide ligand for constructing a molecule based magnet remains unclear.

To evaluate the aptitude of an acetylide ligand for a magnetic material, we tried to construct new molecule-based magnetic materials based on $[CrCyclam(C{\equiv}C\text{-}NaphOMe)_2]^+$ and $TCNQ^-$ (Figure 3a), where the Coulomb repulsion between a negatively charged acetylide ligand and an anion is weakened due to the large π orbital of a naphthyl group and the strong electron affinity of a TCNQ molecule. In consequence, a short contact between an acetylide ligand and a TCNQ anion is expected. The metathesis of $[CrCyclam(C{\equiv}C\text{-}NaphOMe)_2]$ OTf and $Bu_4N^+TCNQ^-$ in 1,2-dichloroethane (DCE) gives $[CrCyclam(C{\equiv}C\text{-}NaphOMe)_2](TCNQ)(DCE)$ (**1**), while the coexistence of a neutral TCNQ gives $[CrCyclam(C{\equiv}C\text{-}Naph OMe)_2](TCNQ)_2(DCE)$ (**2**). The crystal structures of both salts are characterized by the one dimensional alternate stacking of cations and anions ($TCNQ^-$ for **1** or $TCNQ_2^-$ for **2**) as shown in Figure 3b, where naphthyl groups and TCNQ molecules are stacked face-to-face. The magnetic susceptibilities of the salts show good agreement with one dimensional S = [1/2, 3/2] ferrimagnetic model with the intra-chain interaction $2J$ of –19.7 and –4.7 K for **1** and **2**, respectively. These strong interaction via an acetylide ligand evidence the usefulness of transition metal acetylides for a building block of molecule-based magnets.

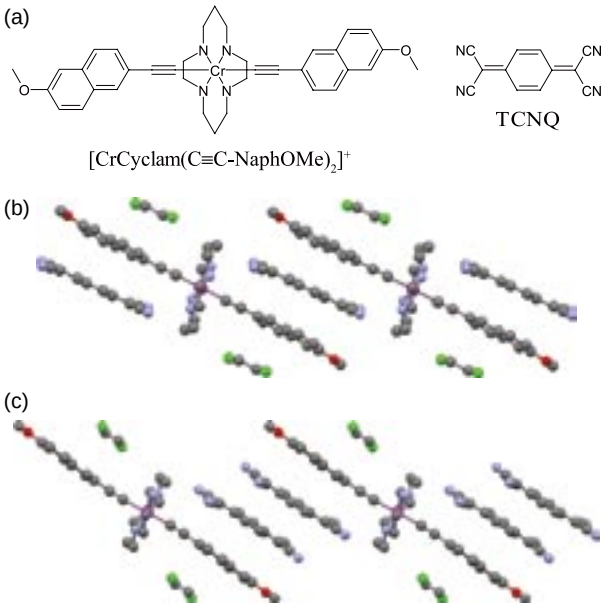

Figure 3. (a): Molecular structures, (b): Crystal structure of **1**, and (c): That of **2**.

Characterization of Magnetic Ultrathin Films by Novel Spectroscopic Methods

Department of Materials Molecular Science
Division of Electronic Structure

YOKOYAMA, Toshihiko	Professor
NAKAGAWA, Takeshi	Assistant Professor
TAKAGI, Yasumasa	Assistant Professor
YAMAMOTO, Isamu	Post-Doctoral Fellow
ISAMI, Kyohei	Graduate Student
EGUCHI, Keitaro	Graduate Student
FUNAKI, Yumiko	Secretary
IWATA, Yumi	Secretary

Novel properties of magnetic metal ultrathin films have been attractive both from fundamental interest and from technological requirements. We are especially interested in drastic modification of metal thin films by surface chemical treatment such as adsorption-induced spin transitions and morphological changes. The magnetic properties are characterized by means of several kinds of spectroscopic methods like MOKE (Magneto-Optical Kerr Effect) using UV-visible lasers and XMCD (X-ray Magnetic Circular Dichroism) using synchrotron radiation soft X-rays.

Moreover, we have been exploiting new techniques based on UV photoemission magnetic circular dichroism (MCD) such as ultrafast time resolved UV MCD photoelectron emission microscopy (PEEM) for spatiotemporal magnetic imaging.

1. Two Opposite Spin Reorientation Transitions in Fe-Covered Ni/Pd(111)[1)]

Magnetic anisotropy has widely been investigated in last decades, and especially perpendicular magnetic anisotropy has attracted much interest because of practical applications to high density recording media. We discovered two opposite spin reorientation transitions (SRTs) in Fe-covered Ni/Pd(111) magnetic films and investigated the origins of the two SRTs.

Pure Ni/Pd(111) films always show in-plane magnetization, irrespective of Ni thickness. Deposition of Fe 1 monolayer (ML) on Ni(6 ML)/Pd(111) causes a transition to perpendicular magnetization, and further Fe 3 ML deposition leads to a return to in-plane magnetization. The first SRT from in-plane to perpendicular magnetization is attributed to a large perpendicular orbital magnetic moment of a single Fe layer, which gives a significant impact on the Fe–Ni interface that stabilizes perpendicular magnetic anisotropy. The second SRT coincides with the structural change in the Fe film from the *fcc* to *bcc* phase, where the reduction in the orbital magnetic moment along the perpendicular direction suppresses the perpendicular magnetic anisotropy stability. It can be proposed that the origin of the second SRT to in-plane magnetization is attributed to cooperative contributions of the structural transformation of the Fe film and the enhanced demagnetizing field.

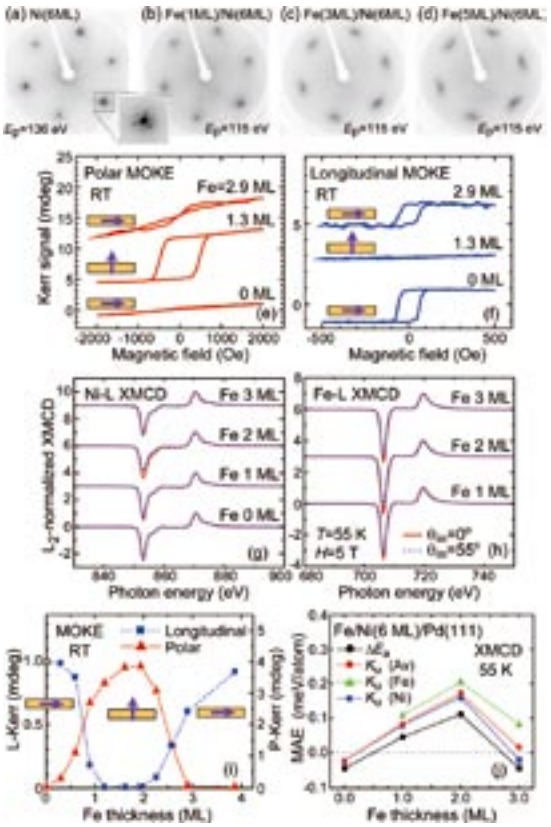

Figure 1. (a-d) Variation of LEED patterns of Ni(6ML)/Pd(111) during Fe deposition up to 5 ML. The structure of Fe changes to *bcc* around 3 ML. (e,f) Typical perpendicular (e) and in-plane (f) magnetization curves of Fe/Ni(6ML)/Pd(111) recorded by polar and longitudinal MOKE, respectively. (g,h) Ni (g) and Fe (h) L-edge XMCD spectra of Fe/Ni(6ML)/Pd(111). (i) Polar and longitudinal MOKE intensities of Fe/Ni(6ML)/Pd(111) as a function of Fe thickness. Two opposite SRTs occur at Fe 1 and 3 ML. (j) Magnetic anisotropy energies estimated by XMCD. The perpendicular magnetic anisotropy is maximized at Fe 2 ML.

Figures 1(a-d) show low energy electron diffraction (LEED) patterns of Ni(6ML)/Pd(111) during Fe deposition. In Ni(6ML)/Pd(111), Moiré spots are clearly visible, implying that Ni is found to grow epitaxially but not pseudo- morphically on Pd(111) with maintaining the inherent Ni–Ni distance. For more than 3 ML Fe deposition, the fundamental spots are elongated, indicating the formation of *bcc* Fe. The structural transformation is concluded to take place around 3 ML Fe.

Figure 1(i) plots the polar and longitudinal MOKE (magneto-optical Kerr effect) intensities at room temperature. It is clearly found that two opposite SRTs occur at Fe 1 and 3 ML, between which the perpendicular magnetization is stabilized. Figures 1(g) and 1(h) exhibit Ni and Fe L-edge XMCD (X-ray magnetic circular dichroism) spectra, which provide spin and orbital magnetic moments and also the microscopic magnetic anisotropy constants as Figure 1(j). The perpendicular magnetic anisotropy is maximized at Fe 2 ML and is subsequently reduced at higher Fe coverage. The second SRT around 3 ML Fe can thus be ascribed to the structural transition to the *bcc* Fe phase, cooperated with the increase in the demagnetization field (shape anisotropy).

2. Observation of One- and Two Photon Photoemission Magnetic Circular Dichroism of Perpendicularly Magnetized Co/Pt(111)

In 2006, we discovered surprising enhancement of the UV-visible photoemission magnetic circular dichroism (MCD) from ultrathin Ni films on Cu(001) when the photon energy was tuned to the work function threshold.[2] Based on this discovery, we succeeded in the first observation of UV MCD PEEM images of ultrathin magnetic films.[3] This method allows us to perform in-laboratory MCD PEEM measurements instead of the usage of third-generation synchrotron radiation XMCD PEEM. Moreover, ultrafast UV MCD PEEM images were successfully obtained by using ultrashort pulsed lasers and a pump-and-probe technique.[4] In 2009, we observed two-photon photoemission (2PPE) MCD and also 2PPE MCD PEEM images from Ni/Cu(001).[5] The 2PPE technique is essentially important for the excitation of deeper valence levels such as semiconductors. In this work, we have exemplified noticeable superiority in 2PPE MCD compared to 1PPE MCD in another example of perpendicularly magnetized Co/Pt(111). This work has been performed under IMS international collaboration program with K. Hild, G. Schönhense and H. J. Elmers (Mainz Johannes Gutenberg-Universität, Germany), and with K. Tarafder and P. M. Oppeneer (Uppsala University, Sweden).

Figure 2(a) shows the LEED pattern of 4.5 ML Co grown on Pt(111). Additional spots can clearly be seen around the fundamental Pt(111) (1×1) spots, which are ascribed to the Moiré patterns from the Co lattice. The Co film is thus found to grow epitaxially but not pseudomorphically on Pt(111). Figure 1(b) depicts the experimental setup. We employed a mode-locked tunable Ti:Sapphire laser (80 MHz, 2.5 W, 680–1020 nm, 100 fs) with the third and fourth-order harmonic

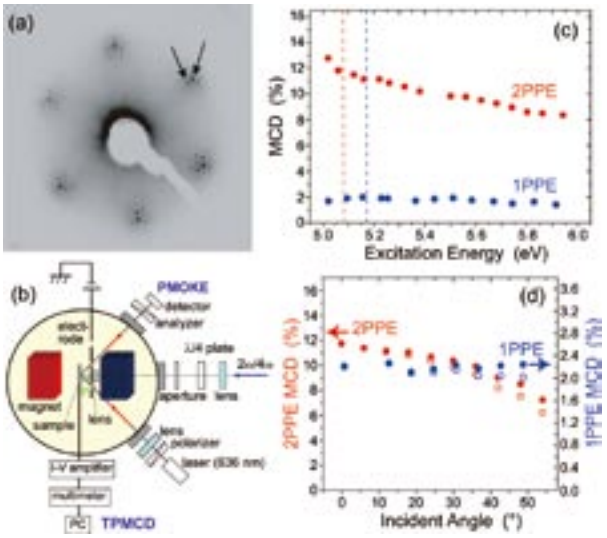

Figure 2. (a) LEED patterns of Co(4.5ML)/Pt(111). (b) 1PPE and 2PPE MCD measurement setup. (c,d) 1PPE and 2PPE MCD asymmetries of Co(4.5ML)/Pt(111) as functions of (c) excitation energy ($h\nu$ and $2h\nu$ for 1PPE and 2PPE, respectively) and (d) the laser incidence angle. The blue and red vertical lines are the work function thresholds, which are slightly different from each other, depending on the sample preparation.

generators. The photoemission from the sample was collected by the anode and the drain sample current was recorded. The sample Co(4.5ML)/Pd(111) shows perpendicular magnetic anisotropy with a coercive field of ~580 Oe.

Figure 1(c) shows the 1PPE and 2PPE MCD asymmetries as a function of the excitation energy. At the work function threshold we obtain maximum values of 1.90% for 1PPE and 11.7% in the case of 2PPE, the latter being as much as 6.2 times larger, elucidating the efficiency of the 2PPE MCD. Figure 1(d) exhibits laser incidence angle dependence of the 1PPE and 2PPE MCD asymmetries. The 2PPE MCD asymmetry is found to be gradually reduced with the increase in the incidence angle, while for 1PPE there is almost no angle dependence observable. These behaviors are significantly different from those of Ni/Cu(001).[5] The measured MCD asymmetries are discussed in two excitation models as well as on the basis of spin-polarized energy-band calculations. The ab initio calculated and measured 1PPE MCD responses are in good agreement. An explanation of the large 2PPE MCD signal is provided in terms of specific inter-band excitations.

References

1) I. Yamamoto, T. Nakagawa, Y. Takagi and T. Yokoyama, *Phys. Rev. B* **81**, 214442 (2010).
2) T. Nakagawa and T. Yokoyama, *Phys. Rev. Lett.* **96**, 237402 (2006).
3) T. Nakagawa, T. Yokoyama, M. Hosaka and M. Katoh, *Rev. Sci. Instrum.* **78**, 023907 (2007).
4) T. Nakagawa, K. Watanabe, Y. Matsumoto and T. Yokoyama, *J. Phys.: Condens. Matter* **21**, 314010 (2009).
5) T. Nakagawa, I. Yamamoto, Y. Takagi, K. Watanabe, Y. Matsumoto and T. Yokoyama, *Phys. Rev. B* **79**, 172404 (2009).

Advanced Design and In-Situ Characterization of Heterogeneous Catalyst Surfaces

Department of Materials Molecular Science
Division of Electronic Structure

TADA, Mizuki	Associate Professor
MURATSUGU, Satoshi	Assistant Professor
NAGAMATSU, Shin-ichi	IMS Resarch Assistant Professor
YANG, Yong	Post-Doctoral Fellow
WENG, Zhihuan	Post-Doctoral Fellow
MAITY, Niladri	Post-Doctoral Fellow
ISHIGURO, Nozomu	Graduate Student*
KUSHIDA, Yuko	Graduate Student*
WANG, Fei	Technical Fellow
FUKUTOMI, Yukiyo	Technical Fellow
UBAHARA, Wakana	Secretary

1. Surface Structure and Catalytic Oxidation Mechanism of SiO_2-Supported Ru Complex Catalyst

Chemical construction of heterogeneous catalyst surfaces on a molecular level toward selective catalysis has been still developing, and the attachment of metal complexes to oxide surfaces is one of the promising ways to create regulated metal structures grafted on oxide surfaces with unique catalytic properties. Stepwise structural transformations of supported metal complexes at surfaces, for instances, chemical grafting, selective ligand elimination, site isolation, surface functionalization, often produce molecularly regulated metal structures efficient for various catalytic reactions. In particular, chemical bonding between metal complexes and support surfaces is one of key issues to create novel metal structures, which are hard to obtain in homogeneous solutions, and anchoring metal complexes to support surfaces also prevents from catalyst deactivation through unfavorable aggregation of metal species under catalytic reaction conditions.

We have prepared a SiO_2-supported Ru-monomer complex coordinating with a *p*-cymene ligand and found that the coordinating *p*-cymene ligand selectively released by an exothermic reaction using a reactant for oxidation reaction (isobutyraldehyde).[1–3] The selective elimination of the *p*-cymene ligand produced a coordinatively unsaturated Ru center, whose structure is presented in Figure 1. The coordinatively unsaturated Ru complex supported on SiO_2 exhibited high activity for aldehyde oxidation and alkene epoxidation.[2]

The SiO_2-supported Ru-monomer complex achieved tremendous TONs (turnover numbers) for the selective oxidation of various aldehydes to corresponding carboxylic acids and alkenes to corresponding epoxides with good conversion and selectivity at ambient temperature, while the homogeneous Ru-precursor complex did not show good catalytic activity for both oxidation reactions. For examples, the TON of 38,800,000 for selective isobutyraldehyde (IBA) oxidation was achieved with the selectivity of 94% and the TON of 2,100,000 for *trans*-stilbene epoxidation using IBA/O_2 was achieved with the selectivity of 90%. Furthermore, the SiO_2-supported Ru catalyst could be recycled by simple filtration and both conversion and selectivity were still constant for several runs. Ru K-edge EXAFS analysis after the selective oxidation reactions indicated the high stability of the SiO_2-supported Ru complex catalyst under the catalytic oxidation conditions.

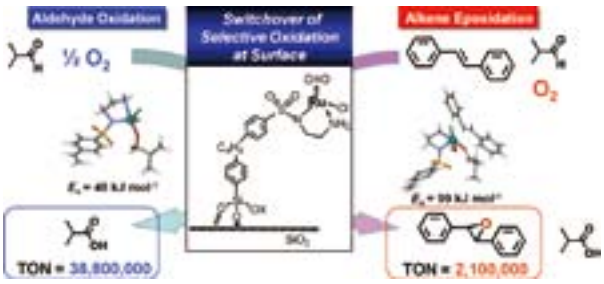

Figure 1. Switchover of selective catalytic oxidation reactions on the SiO_2-supported Ru complex catalyst.

We also found that the IBA sole oxidation with O_2, whose activation energy was 48 kJ mol^{-1} and was much smaller than that of the *trans*-stilbene epoxidation using IBA and O_2 (99 kJ mol^{-1}), was suppressed by the coexistence of *trans*-stilbene. During the catalytic epoxidation of *trans*-stilbene, co-existing IBA was stoichiometrically consumed for the epoxidation, and the facile IBA sole oxidation was found to be negligible. The switchover of the selective oxidation pathways from the IBA sole oxidation to the *trans*-stilbene epoxidation using IBA was explained in terms of energy profiles for the alternative selective oxidation pathways calculated by DFT, suggesting the preferential coordination of *trans*-stilbene to the active Ru complex at the surface.

2. Preparation, Characterization, and Shape-Selective Catalytic Performances of Molecularly Imprinted Ru-Complex Catalysts

Molecular imprinting of a supported metal complex whose ligand serves as a prescribed template is devoted to the design of shape-selective reaction space with a similar shape to the template. A molecularly imprinted cavity memorized the shape and coordination environment of the template ligand can be prepared on an unsaturated active metal center behind the template from the supported metal complex. We have designed and prepared a molecularly imprinted Ru-complex catalyst on SiO_2 and succeeded in regulating the regio- and shape-selective epoxidation of limonene.

A molecularly imprinted Ru-complex catalyst was prepared by step-by-step procedures: (1) the attachment of a Ru complex on SiO_2, (2) the coordination of limonen-10-ol (template), which possesses a similar shape to an intermediate of terminal C=C bond epoxidation of limonene, (3) stacking of surface SiO_2-matrix overlayers, and (4) the removal of the template ligand from the Ru site. The structures of the supported and molecularly imprinted Ru catalysts were characterized by solid-state NMR, FT-IR, XRD, XRF, UV/vis, BET, and Ru K-edge XAFS.

We found that the molecularly imprinted Ru catalyst designed for the terminal C=C bond epoxidation of limonene exhibited fine shape selectivity discriminating a methyl group of alkene reactants and high regioselectivity for the limonene epoxidation. Internal epoxide (62% selectivity) was preferably obtained on the supported Ru catalyst, while the molecularly imprinted Ru catalyst produced terminal epoxide of limonene with 63% selectivity. We found that the selectivity for the terminal epoxide increased to 90% and that for the internal epoxide decreased to 9% when SiO_2-matrix overlayers were prepared by the addition of 1.0 wt% 3-(2-imidazolin-1-yl)-propyltriethoxysilane to $Si(OCH_3)_4$ (TMOS). The basic compound was suggested to promote the hydrolysis-polymerization of TMOS, as a result, fine imprinted cavity for the limonene epoxidation was suggested to be prepared.

We have also designed novel molecularly imprinted Ru catalysts for the asymmetric transfer hydrogenation of ketones. An NH_2 binding site was spatially arranged on the wall of molecularly imprinted matrix overlayers as shown in Figure 2. A template ligand (**B**) with a carbamate moiety was coordinated to a SiO_2-supported Ru complex (**A**). (**B**) is composed of three parts: (**a**) *o*-hydroxybenzhydrol moiety, which is a molecularly imprinted structure and has a similar shape to the product of *o*-fluorobenzophenone (*o*-F-BP), (**b**) a carbamate moiety (–NHCOO–), and (**c**) a 3-triethoxysilylpropyl (–Si$(OC_2H_5)_3$) branch. Then, SiO_2-matrix overlayers were stacked by the chemical vapour deposition and during the subsequent hydrolysis- polymerization of TMOS, the branch ((**B**)-(**c**)) was taken in the wall of the SiO_2-matrix overlayers. Finally, the carbamate moiety ((**B**)-(**b**)) was broken to $–NH_2$, CO_2, and –OH, and then the coordination of (**B**)-(**a**) was removed to prepare the molecularly-imprinted Ru catalyst (**C**). The NH_2 binding site originally coordinated to the imprinted template (**B**)-(**a**) was fixed on the wall of the SiO_2-matrix overlayers and is regarded to be coordinated to the F-substituent of *o*-F-BP by hydrogen bonding. The molecularly imprinted cavity acted as an efficient reaction space for the shape-selective transfer hydrogenation of *o*-F-BP.

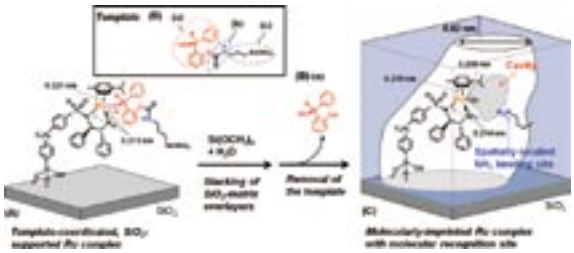

Figure 2. Design of a molecularly imprinted Ru-complex catalyst with a molecular binding site for asymmetric transfer hydrogenation of *o*-F-BP.

References

1) M. Tada, Y. Akatsuka, Y. Yang, T. Sasaki, M. Kinoshita, K. Motokura and Y. Iwasawa, *Angew. Chem., Int. Ed.* **47**, 9252–9255 (2008).
2) M. Tada, S. Muratsugu, M. Kinoshita, T. Sasaki and Y. Iwasawa, *J. Am. Chem. Soc.* **132**, 713–724 (2010).
3) M. Tada, *Bull. Chem. Soc. Jpn.* **83**, 855–876 (2010) (Award Accounts).

Awards

TADA, Mizuki; Presentation Award for Young Researcher (Catalysis Society of Japan).
TADA, Mizuki; 2010 The Young Scientist's Prize of The Commendation for Science and Technology by the Minister of Education, Culture, Sports, Science and Technology, Japan.
MURATSUGU, Satoshi; The 26th Inoue Research Award for Young Scientists (Inoue Foundation for Science).
MURATSUGU, Satoshi; CSJ Presentation Award 2010 (The Chemical Society of Japan).
MURATSUGU, Satoshi; The Royal Society of Chemistry Poster Prize (Japan-UK Symposium: Catalysis for a Sustainable World).

* carrying out graduate research on Cooperative Education Program of IMS with The University of Tokyo

Optical Studies of Charge Ordering in Organic Conductors

Department of Materials Molecular Science
Division of Electronic Properties

YAKUSHI, Kyuya	Professor
YAMAMOTO, Kaoru	Assistant Professor
URUICHI, Mikio	Technical Associate
YUE, Yue	Post-Doctoral Fellow
ABE, Hitomi	Secretary

In organic conductors, kinetic energy is comparable with on-site and inter-site Coulomb energy. Due to this reason, many organic conductors are located in a boundary area between metallic and localized states, and thus various organic charge-transfer compounds show metal–insulator phase transition. Recently, charge-ordered (CO) state originated from Coulomb interaction is widely found in organic conductors, and the electronic phase diagrams of typical organic conductors are re-considered taking CO into account. The CO state attracts much attention, first because charge-mediated superconductivity is theoretically predicted in superconducting compounds neighbored on CO phase, second because some compounds in CO phase show ferroelectricity through the crystallization of conduction electrons. We have investigated the CO state and metallic state near CO employing infrared and Raman, and reflection spectroscopy.

1. Nonuniform Site-Charge Distribution and Fluctuations of Charge Order in the Metallic State of α-(BEDT-TTF)$_2$I$_3$[1)]

Among a variety of organic conductors, the α-(BEDT-TTF)$_2$I$_3$ shows rich properties such as charge order, superconductivity, zero-gap state, persistent photoconductivity, photo-induced phase transition, and non-linear optical response. This compound exhibits a first-order metal–insulator (MI) phase transition at T_{MI} = 135 K. The MI transition is considered to be driven mainly by on-site and intersite Coulomb interaction. Based on theoretical, ^{13}C-NMR, Raman, and x-ray studies, the insulating phase is regarded as a charge-ordered state involving a moderate structural change. First, we have quantitatively examined the amplitude of charge order below T_{MI} based on the rational assignment of the charge-sensitive C=C stretching modes. Compared with the insulating phase, the metallic phase of α-(ET)$_2$I$_3$ has not been thoroughly investigated, although the electronic structure of the metallic phase is related to the superconductivity under uniaxial strain, zero-gap state under hydrostatic pressure, and the excited state

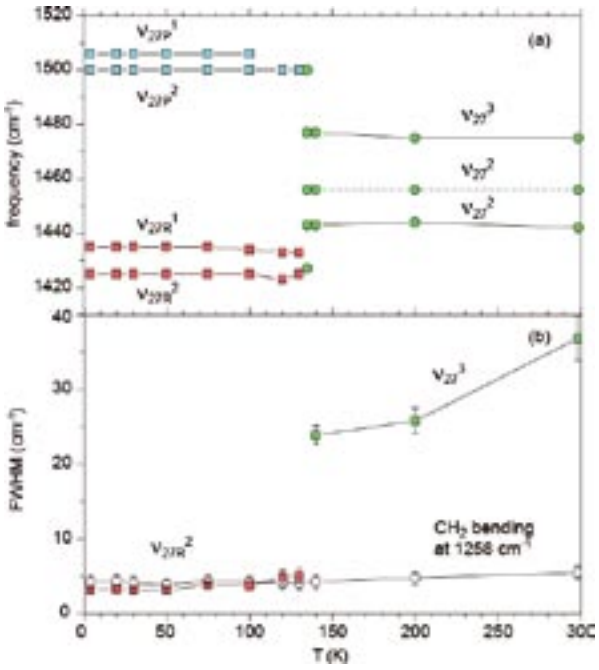

Figure 1. (a) Frequencies of ν_{27} modes (C=C stretching) plotted against temperature. The three ν_{27} mode largely split into two groups (charge-rich and charge-poor sites) (b) Temperature dependence of the linewidth (FWHM) of the ν_{27}^3 (green square) mode, which involves weak ν_{27}^2, and ν_{27R}^2 (orange square) modes. The temperature dependence of the CH2 bending mode (open circle) at 1258 cm^{-1}, the frequency of which is insensitive to site charge, is shown for comparison.

of the photo-induced metal–insulator transition. Second, we have analyzed the linewidth of the charge-sensitive C=C stretching mode, and found a thermally activated short-range charge oder in the metallic phase above T_{MI}.

Figure 1 shows the splitting and linewidth of the infrared-active charge-sensitive mode, ν_{27}. Below T_{MI}, these modes are largely split into two groups, which correspond to the two charge-rich and two charge-poor sites. From the relationship

between the frequency and site charge, the site charge is deduced to be (0.8_1, 0.7_4, 0.2_6, and 0.2_3). The linewidth of these modes is narrow (~4 cm^{-1}) as shown in Figure 1b. The large amplitude and narrow linewidth below T_{MI} unambiguously indicates the charge-ordered state with long-range order. In the metallic phase above T_{MI}, this mode is split into three. The site-charge is deduced to be (0.6_8, ~0.6, and 0.4_4). We interpret this small amplitude of site-charge distribution is caused by the distribution of transfer integrals. The most important difference between metallic and charge ordered phases is the linewidth as shown in Figure 1b. We interpret the very broad linewidth as the fluctuation of site charge. Assuming the Gaussian process for the fluctuation, the fluctuation rate was estimated to be 1–25 cm^{-1}. This slow fluctuation rate suggests a collective motion of short-range ordered charge-ordering stripe. We propose that several short-range ordered charge-ordering stripes are thermally activated in the metallic phase. This idea is consistent with the entropy driven first order MI phase transition. The optical conductivity in the metallic phase obtained from the analysis of reflectivity shows no Drude response, which may be associated with this fluctuation of charge order. According to the high-pressure experiment, this charge-ordering fluctuation is well suppressed.

2. Vibronic Activation of Vibrational Overtone in the Infrared Spectrum of Charge-Ordered Organic Conductors[2)]

Infrared spectrum provides us important knowledge on the valence states in strongly correlated systems. However, there is substantial difficulty in the analysis of the spectrum, because the valence electrons in these systems are affected by various interactions such as electron–electron or electron–phonons, complicating the interpretation of the spectral signals. For instance, even a phonon signal, which has the chemically defined frequency, is difficult to assign unambiguously because of large frequency-shift due to strong vibronic coupling.

In the study, we focused on the identification of the dip-shaped anomaly appearing in the infrared spectrum of a group of organic conductors (the highlighted region in Figure 2). The anomaly appears at approximately the same frequency (*ca.* 2700 cm^{-1}), irrespective of the substances when they transform to charge-ordered phase. By the isotope-shift measurement performed for θ-(BEDT-TTF)$_2$RbZn(SCN)$_4$, we found that there is a relevance of the anomaly to the overtone of a C=C stretching mode of BEDT-TTF molecule. From the fact that the dip is observed exclusively for the materials showing charge ordering, it is suggested that that the anharmonicity activating the overtone does not exist in the potential of individual molecules; instead we suppose, which should be in the electronic potential formed by intermolecular vibronic interactions.

For organic conductors, the electronic potential depends strongly on molecular vibrations *via* the vibronic interaction called electron–molecular vibration (e–mv) coupling. The vibronic phenomenon has been explained within the frame-

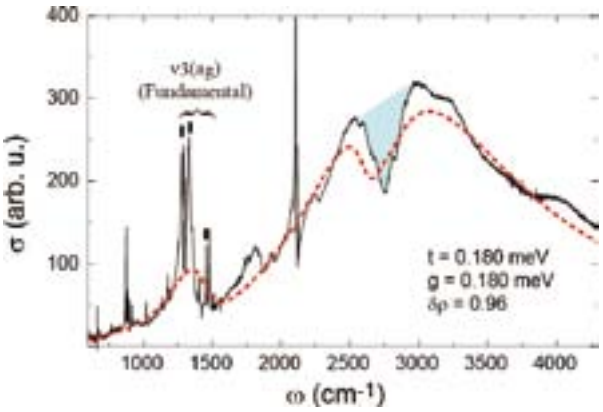

Figure 2. The comparison of the numerical result (dotted line) to the experimentally obtained optical conductivity of θ-(BEDT-TTF)$_2$RbZn(SCN)$_4$ [*E*//*a*, *T* = 6 K] (solid line). (The parameters used in the calculations: $\omega_{neutral}$ = 1494 cm^{-1}, ω_{cation} = 1407 cm^{-1}, line-width of molecular mode: 100 cm^{-1}, linewidth of electronic transition: 1000 cm^{-1}, *t* = 180 meV, e–mv coupling constant: 180 meV) The highlighted region denotes the dip-shape anomaly, whereas the sharp peaks labeled by the ticks are the fundamental signals of $\nu_3(a_g)$.[3)]

work of a linear-coupling theory, in which the coupling effect is treated as an energy shift of the valence level. The aim of the present study is to extend the linear-coupling theory to explain the activation mechanism of the overtone of a vibrational mode that behaves otherwise a harmonic oscillator.

We calculated the corrections of the adiabatic electron potential due to the vibronic coupling to higher-ordered terms using a diatomic molecular dimer model. Additionally, the dynamic susceptibility was calculated using the same model. The main arguments derived from the study are summerized: (1) In the energy corrections, there appear two cubic terms—the lowest-order anharmonicity—in terms of the molecular coordinates. (2) One of them is connected with charge separation between the two molecules, which term presumably induces the anharmonicity activating the overtone. (3) The vibronically induced anharmonicity arises from the nonlinearity in the adiabatic mixing of the electronic levels in accordance with charge separation. (4) Essential features of the experimentally obtained spectrum were reproduced by the numerical calculation of the dynamical susceptibility based on the cluster mode (Figure 2). (5) There is an intimate relationship between the activation of the overtone and nonlinear electric susceptibility; actually we have demonstrated that an organic conductor α-(BEDT-TTF)$_2$I$_3$, which shows the overtone signal along with charge ordering, generates strong second-order optical nonlinearity.[4)]

References

1) Y. Yue, *et al.*, *Phys. Rev. B* **82**, 075134 (2010).
2) K. Yamamoto, *et al.*, submitted.
3) K. Yamamoto *et al.*, *Phys. Rev. B* **65**, 085110 (2002).
4) K. Yamamoto, *et al.*, *J. Phys. Soc. Jpn.* **77**, 074709 (2008).

Magnetic Resonance Studies for Molecular-Based Conductors

Department of Materials Molecular Science
Division of Electronic Properties

NAKAMURA, Toshikazu	Associate Professor
FURUKAWA, Ko	Assistant Professor
IWASE, Fumitatsu	IMS Fellow
SUGIURA, Koichi	Graduate Student
ABE, Hitomi	Secretary

Magnetic resonance measurements are advantageous for studying fundamental electronic properties and for understanding the detailed electronic structures of molecular based compounds. Developing an understanding of the electronic phases and functionality of these materials enables us to perform systematic investigations of low-dimensional, highly-correlated electron systems and functional materials. Competition between the electronic phases in molecular-based conductors has attracted much attention. The investigations of such electronic phases by magnetic resonance measurements are important to understanding unsolved fundamental problems in the field of solid state physics, and to explore novel functionalities in the field of material science.

In this study, we performed broad-line NMR and ESR measurements on molecular-based conductors to understand electron spin dynamics and functionality in low-temperature electronic phases.

1. Anomalous Temperature Dependence of *g*-Tensor in Organic Conductor, $(TMTTF)_2X$ (X = Br, PF_6 and SbF_6)

The magnetic properties of organic conductor $(TMTTF)_2X$ (X = Br, PF_6 and SbF_6), where TMTTF is tetramethyltetrathia fulvalene, were examined by electron spin resonance (ESR) spectroscopy, X-ray diffraction (XRD) of the single crystals, and quantum-chemical calculation of the *g*-tensor. In the case of salts with bulky counter anions such as the PF_6 and SbF_6, an anomalous temperature dependence of the *g*-tensor was observed in the temperature range from 20 K to 296 K. This anomalous behavior of the *g*-tensor signifies the rotation of the principal axes as well as the shift of the principal values. The *g*-tensor of the Br salt is, however, temperature independent. No remarkable change in the intra-molecular structure as a function of temperature was observed for all salts. On the other hand, the distance between TMTTF and counter-anion molecules obviously decreases as the temperature decreases for the PF_6 and the SbF_6 salts, while thermal contraction is not remarkable for the Br salt. In order to clarify the origin of the anomalous behavior of the *g*-tensor, we investigated the possibility of deformation of the wave-function by the counter-anion potentials using a quantum-chemical calculation for the actual crystal structures measured at low-temperatures. In this paper, we describe the first direct observation of the deformation of the frontier orbital by the counter anion potential for organic conductors. The intra-molecular spin-distribution as a function of temperature also is discussed from the microscopic point of view.

2. Electronic Properties of a TMTTF-Family Salt, $(TMTTF)_2TaF_6$: New Member Located on the Modified Generalized Phase-Diagrams

A new TMTTF-family salt, $(TMTTF)_2TaF_6$, which has the largest octahedral (Oh) symmetry counter anion among the various salts in the TMTTF family, was prepared. X-ray, static magnetic susceptibility, Electron Spin Resonance (ESR) and Nuclear Magnetic Resonance (NMR) measurements were carried out in order to investigate the electronic state of $(TMTTF)_2TaF_6$. The unit-cell volume of $(TMTTF)_2TaF_6$ is larger than that of $(TMTTF)_2MF_6$ (M = P, As and Sb). $(TMTTF)_2TaF_6$ shows the highest charge-ordering phase transition temperature (T_{CO} ~ 175 K) among TMTTF salts with the Oh-symmetry counter anion. These facts indicate that $(TMTTF)_2TaF_6$ is located on the most negative side in the generalized phase-diagram for TMT*C*F family salts. $(TMTTF)_2TaF_6$ undergoes an antiferromagnetic transition around 9 K. It turned out the phase diagram needs to be modified.

3. Spin-Dynamics in Vicinity of Phase Transition for Organic Conductor $(TMTTF)_2X$

The spin dynamics in the vicinity of the spin-gap phase transition for the organic conductor $(TMTTF)_2PF_6$ were examined by pulsed-ESR spectroscopy. An anomaly in the

relaxation time was observed in the intermediate region between the ground state and the high-temperature phase and was associated with the charge re-orientation originating in the transverse magnetic interaction. The calculation of the overlap integrals implied considerable inter-chain interactions. The transverse magnetic interaction plays an important role of the spin-gap phase transition in $(TMTTF)_2PF_6$.

4. Novel Type of Career Generated System: Magnetic Investigations of TTF-Based Self-Doped Hydrogen-Bonding Conductor

Magnetic investigations, including static magnetic susceptibility and high-field Electron Spin Resonance (ESR) measurements, were carried out for an organic conductor, $(TTFCOO)[(NH_4^{+1})_{1-x}(NH_3)_x]$. Anisotropic ESR parameters were determined for powder samples using a high-frequency W-band (93.9817 GHz) ESR spectrometer. The observed principal values of the *g*-tensor and quantum chemical calculation results indicate that the observed spin is distributed on quasi-hole-like TTF skeletons, and that the TTFCOO mainframe partially becomes a neutral radical. The temperature dependence of the spin susceptibility is well fitted with a Curie-Weiss term and an activation-type term, with the activation-type term dominant at high temperatures. The high absolute value of the spin susceptibility and the extremely small activation energy, Δ, indicate that a quasi-degenerate (metallic) state is stabilized in $(TTFCOO)[(NH_4^{+1})_{1-x}(NH_3)_x]$, although the weakly temperature-dependent ESR linewidth indicates a localized characteristic. A novel type of carrier generation, self-doping, was discussed.

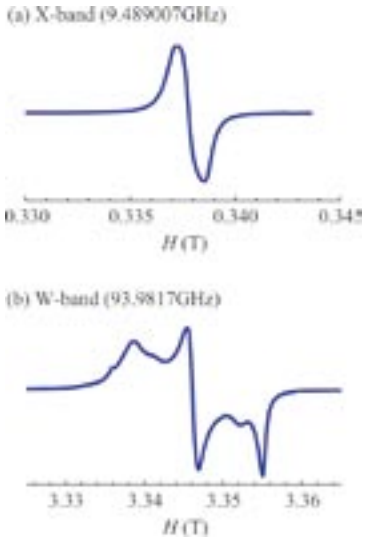

Figure 1. Typical ESR spectra for powder $(TTFCOO)[(NH_4^{+1})_{1-x}(NH_3)_x]$ (at 100 K) using the (a) X-band (93.9817 GHz), and (b) W-band (93.9817 GHz), frequency regions.

5. The Ground States and Critical Behavior in the Quasi-One-Dimensional Complexes $(TMTTF)_2[(AsF_6)_x(SbF_6)_{1-x}]$

^{13}C NMR measurements were carried out to understand the chemical pressure effect on the ground state in quasi-one-dimensional (1D) organic complexes using the alloy system $(TMTTF)_2[(AsF_6)_x(SbF_6)_{1-x}]$ (x ~ 0.3, 0.5, 0.67). The temperature of the charge-ordering transition decreases with the concentration of AsF_6. Additional line splitting and the rapid increase in the spin-lattice relaxation rate, $1/T_1$, on cooling for the salt of x ~ 0.3 indicates that the ground state of the salt is antiferromagnetic. In the x ~ 0.67 alloy, the spin gap opens without antiferromagnetic spin correlations. The intermediate salt of x ~ 0.5 is located in the vicinity of the quantum critical region between two phases at low temperatures. The quasi-1D correlation and antiferromagnetic critical behavior are discussed in terms of the power-law behavior of $1/T_1$.

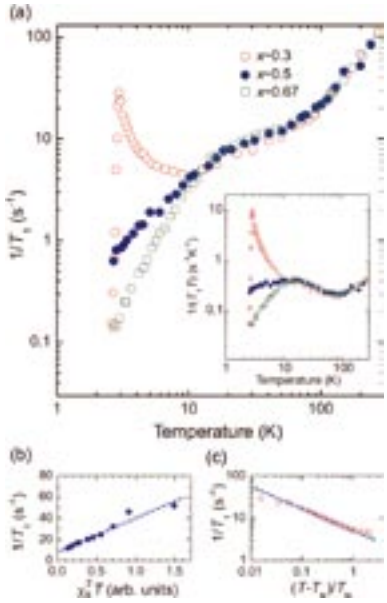

Figure 2. a) Temperature dependence of $1/T_1$. The inset shows the temperature dependence of $1/(T_1T)$. (b) $1/T_1$ as a function of χ_S^2T for the alloy of x ~ 0.5. (c) Power-law behavior of $1/T_1$ for the alloy of x ~ 0.3 on approaching T_N by lowering temperature.

References

1) K. Furukawa, T. Hara and T. Nakamura, *J. Phys. Soc. Jpn.* **78**, 104713 (6 pages) (2009).
2) F. Iwase, K. Sugiura, K. Furukawa and T. Nakamura, *J. Phys. Soc. Jpn.* **78**, 104717 (7 pages) (2009).
3) K. Furukawa, T. Hara and T. Nakamura, *J. Phys. Soc. Jpn.* **79**, 043702 (4 pages) (2010).
4) K. Furukawa, T. Nakamura, Y. Kobayashi and T. Ogura, *J. Phys. Soc. Jpn.* **79**, 053701 (4 pages) (2010).
5) F. Iwase, K. Sugiura, K. Furukawa and T. Nakamura, *Phys. Rev. B* **81**, 245126 (6 pages) (2010).

Award

SUGIURA, Koichi; Tokai-Branch, Chemical Society of Japan Award.

Conjugated Microporous Polymers—A New Class of Porous Frameworks for Function Design

Department of Materials Molecular Science
Division of Molecular Functions

JIANG, Donglin	Associate Professor
KOU, Yan	Post-Doctoral Fellow
CHEN, Long	Post-Doctoral Fellow
XU, Yanhong	Graduate Student
DING, Xuesong	Graduate Student
FENG, Xiao	Graduate Student*
SUZUKI, Hiroko	Secretary

Conjugated microporous polymers (CMPs) are a new class of porous materials with amorphous three-dimensional organic framework. Unlike other porous materials, CMPs are unique in that they enable the elaborate integration of π-electronic components to the covalent framework while retaining a permanent porous structure. Most studies on CMPs to date have focused on the development of synthetic approaches for the control of pore size and surface area. However, the functions of CMPs, apart from gas storage, have not yet been well explored. We have focused on the development of functional CMPs via molecular design of the CMP skeletons.

1. Light-Harvesting Conjugated Microporous Polymers: Rapid and Highly Efficient Flow of Light Energy with a Porous Polyphenylene Framework as Antenna

The molecular design of light-harvesting antennae requires not only the segregation of a large number of chromophore units in a confined nanospace but also the cooperation of these units in achieving highly efficient energy transduction. We have focused on the development of photofunctional CMPs with the expectation that the energy-donating CMPs with dense π-electronic components could serve as antennae for the collection of photons, while inherent pores within the framework could spatially confine energy-accepting counterparts, thus leading to the creation of an unprecedented donor–acceptor system for energy transduction mediated by the three-dimensional porous framework.

Here we report the synthesis and functions of a polyphenylene-based conjugated microporous polymer (Figure 1, PP-CMP). PP-CMP was recently designed and synthesized by Suzuki polycondensation reaction and used as antenna for the noncovalent construction of light-harvesting system. In contrast to linear polyphenylene, PP-CMP consists of conjugated three-dimensional polyphenylene scaffolds and holds inherent porous structure with uniform pore size (1.56 nm) and large surface area (1083 m^2 g^{-1}). It emits blue photoluminescence, is capable of excitation energy migration over the framework, and enables rapid transportation of charge carrier with intrinsic

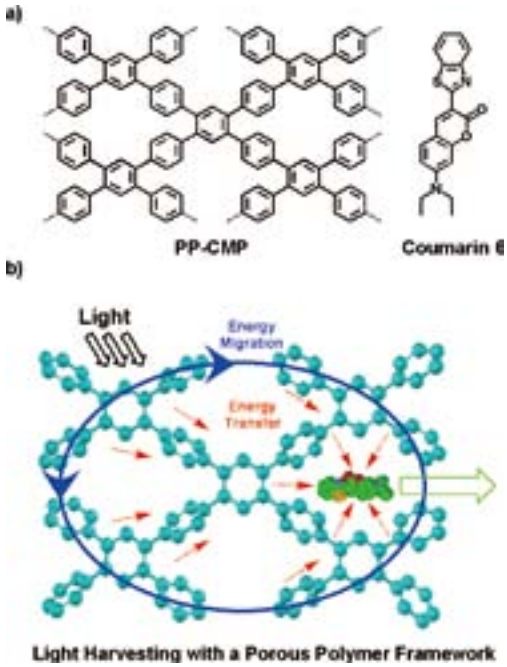

Figure 1. Schematic representations of (a) the synthesis and (b) the framework of PPy-COF (Structure is based on quantum calculation and crystal lattice parameters; Red: B, White: O, Blue: Pyrene; H atoms are omitted for clarity).

mobility as high as 0.04 $cm^2V^{-1}s^{-1}$. The microporous structure of PP-CMP allows for the spatial confinement of energy-accepting coumarin 6 molecules in the pores and makes the high throughput synthesis of light-harvesting systems with designable donor–acceptor compositions possible. Excitation of PP-CMP skeleton leads to brilliant green emission from

coumarin 6, whose intensity is 21 fold as high as that upon direct excitation of coumarin 6 itself; while the fluorescence from PP-CMP itself is wholly quenched, as a result of energy transfer from the light-harvesting PP-CMP framework to coumarin 6. PP-CMP skeleton is highly cooperative with averagely 176 phenylene units working together to channel the excitation energy to one coumarin 6 molecule and features the energy transfer process with quick, efficient and vectorial character. These unique characteristics clearly originate from the conjugated porous structure and demonstrate the usefulness of CMPs in the exploration of π-electronic functions, in addition to their gas adsorption properties thus far reported. The light-harvesting antennae based on CMPs constitutes an important step for molecular optoelectronics based on porous polymeric materials.

2. CMPs as Scaffolds for Constructing Porous Catalytic Frameworks: A Built-In Heterogeneous Catalyst with High Activity and Selectivity Based on Nanoporous Metalloporphyrin Polymers

Recently, CMPs have been developed to load metal nanoclusters for the synthesis of heterogeneous catalysts. Because the polymer skeleton does not incorporate any catalytic sites, post treatment of CMPs via noncovalent interactions is a prerequisite for loading catalysts in the pores. In contrast to this approach, we are interested in the exploration of covalently built-in catalysis systems based on CMPs. If catalytic functionalities could be integrated into the skeleton of CMPs, one would have a chance to create a novel porous polymer in which the skeleton itself serves as the catalysts and the pores provide spaces for the transformation. Here we report a strategy for the synthesis of a new type CMP-based heterogeneous catalyst that consists of an inherent porous framework with built-in catalytic sites in the skeleton (Figure 2, FeP-CMP).

FeP-CMP was newly synthesized *via* a Suzuki polycondensation reaction and was developed as a heterogeneous catalyst for the activation of molecular oxygen to convert sulfide to sulfoxide under ambient temperature and pressure. FeP-CMP is intriguing because the polymer skeleton itself is built from catalytic moieties and serves as built-in catalysts, bears inherent open nanometer-scale pores that are accessible for substrates, and possesses high surface areas (1270 m^2 g^{-1}) that facilitate the transformation reaction. It is highly efficient with high conversion (up to 99%) and large turnover number (TON = 97,320), is widely applicable to various sulfides covering from aromatic to alkyl and cyclic substrates, displays high selectivity (up to 99%) to form corresponding sulfoxides, and is highly chemoselective for the oxidation of sulfide group even in the co-existence of other oxidative functionalities. Owing to the covalent linkages between catalytic sites in the frameworks, FeP-CMP can be recycled with good retention of its porous structure and allows for large-scale transformation. These unique characteristics clearly originate from the covalent porous catalytic framework structure and demonstrate the usefulness of CMPs in the exploration of built-in heterogeneous catalysts, a new potential of these materials that have thus far been reported to exhibit noteworthy gas adsorption functions.

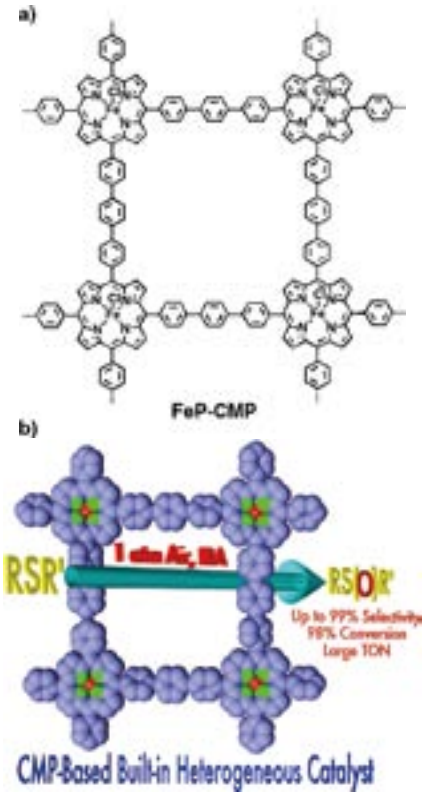

Figure 2. a) Schematic representation of the nanoporous polymer with metalloporphyrin built-in skeleton (FeP-CMP). b) Schematic representation of the transformation of sulfides to sulfoxides catalyzed by FeP-CMP.

Exploration of conjugated microporous polymers has a high probability of leading to the development of new functional materials. In summary, we developed a novel strategy for the construction of built-in catalysts based on CMPs architecture and demonstrated the utility of a newly synthesized FeP-CMP as a heterogeneous catalyst. A clear future potential for CMPs is to develop photocatalyst in which multiple functions including light-harvesting, energy transfer and catalytic processes can be seamlessly merged in one polymer skeleton. Therefore, the CMPs-based built-in catalyst constitutes a new step for the molecular design of heterogeneous catalyst systems.

References

1) L. Chen, Y. Honsho, S. Seki and D. Jiang, *J. Am. Chem. Soc.* **132**, 6742–6748 (2010).
2) L. Chen, Y. Yang and D. Jiang, *J. Am. Chem. Soc.* **132**, 9138–9143 (2010).

* from Beijing Institute of Technology

Structural Biology Based on Solid State NMR Spectroscopy

Department of Materials Molecular Science
Division of Molecular Functions

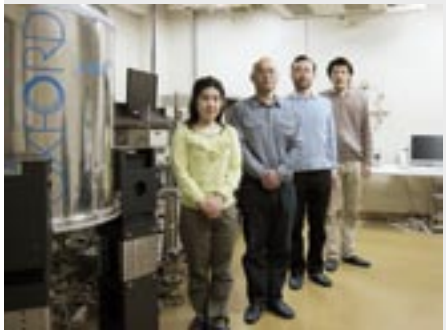

NISHIMURA, Katsuyuki	Associate Professor
IIJIMA, Takahiro	Assistant Professor
TANIO, Michikazu	IMS Research Assistant Professor

Solid state NMR is one of the useful tools to characterize dynamics and structures of molecules on amorphous condition without specific limitations. We are working on methodology developments of solid state NMR for structural biology and material science. Especially, we are focusing on elucidation of functions and dynamic structure of peripheral membrane protein bound to lipid bilayer surface based on solid state NMR. In the following, we show the new lipid sample system enabling magnetically aligned planer lipid bilayers useful for structural characterization of peripheral membrane proteins. In addition, a study of molybdenum compounds was reported.

1. Bicelle:Magnetically Aligned Planner Lipid Bilayers at Room Temperature for Structural Characterization of Membrane Bound Proteins by Solid State NMR

The properly hydrated mixture of saturated lipids possessing short and long acyl-chains at proper composition forms planer lipid bilayer so called bicelle which can be magnetically aligned under static magnetic field at temperature from 30 to 40 °C and widely used in solid state NMR for structural characterization of membrane associated proteins. Last year, we reported that addition of proper amount of phosphatidylinositol 4, 5-bisphosphate (PIP_2) into bicelle significantly enhances the stability of magnetic alignment and increases its temperature range of magnetic alignment. Those effects were demonstrated for the bicelle proposed by Triba *et al.*, enabling magnetic alignment at room temperature. This bicelle composes mixture of saturated lipid 1,2-dimyristoyl-*sn*-glycero-3-phosphocholine (DMPC) and unsaturated lipid 1-palmitoyl-2-oleoyl-*sn*-glycero-3- phosphocholine (POPC) for long acyl chain, and 1,2-dihexanoyl-*sn*-glycero-3-phosphocholine (DHPC) for short acyl chain lipid, respectively.

In this study, we have identified the origin of enhancement of magnetic alignment due to addition of PIP_2 into bicelle.

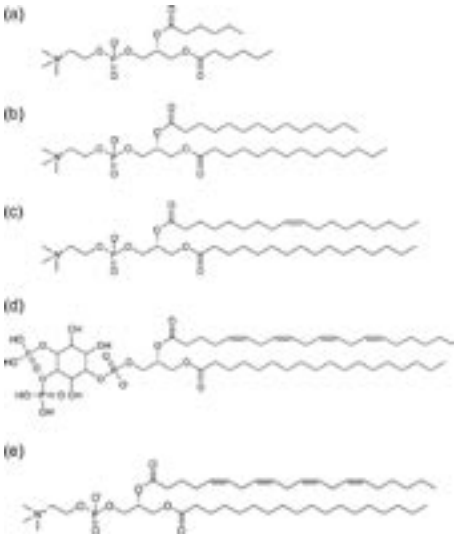

Figure 1. Molecular structures for (a) DHPC, (b) DMPC, (c) POPC, (d) PIP_2, and (e) SAPC, respectively.

Orientational properties of bicelles prepared from the different composition of lipids were verified based on ^{31}P-NMR.1-stearoyl-2-arachidonoyl-*sn*-glycero-3-phosphocholine (SAPC) has the polar head and the acyl chains as same molecular structure as those for DMPC and PIP_2, respectively. The bicelle composing SAPC instead of PIP_2 at same molar ratio was prepared in order to indentify either polar head group or acyl-chains of PIP_2 contributing to the enhancement of magnetic alignment of bicelle. Figure 1 shows the ^{31}P-NMR spectra for the bicelle prepared from (a) PIP_2/POPC/DMPC/DHPC, (b) POPC/DMPC/DHPC, and (c) SAPC/POPC/DMPC/DHPC for the temperature range from 12 to 22 °C. The peaks around –3 and –11 ppm are originated from DHPC and POPC/DMPC mixture, respectively. The peak around –15.5 ppm is $\delta_\perp$ edge of axially symmetric powder pattern of ^{31}P chemical shift anisotropy from multi lamella vesicles (MLVs). PIP_2/

POPC/DMPC/DHPC-bicelle was magnetically aligned stably from 14 to 20 °C. In contrast, POPC/DMPC/DHPC-bicelle was magnetically aligned only at 16 °C. At 18 °C, $\delta_{\perp}$ edge of axially symmetric powder pattern of ^{31}P chemical shift anisotropy from MLVs was appeared. SAPC/POPC/DMPC/DHPC-bicelle exhibited insufficient magnetic alignment over measured temperature range.

From the comparison of ^{31}P-NMR spectra for those bicelles, it is obvious that addition of SAPC into POPC/DMPC/DHPC-bicelle dose not enhance magnetic alignment. Thus we concluded that inositol 4, 5-bisphosphate residue in PIP_2 may contribute to the enhancement of magnetic alignment of bicelle. Our results may give the way to design new reagents to enhance magnetic alignment of bicelle.

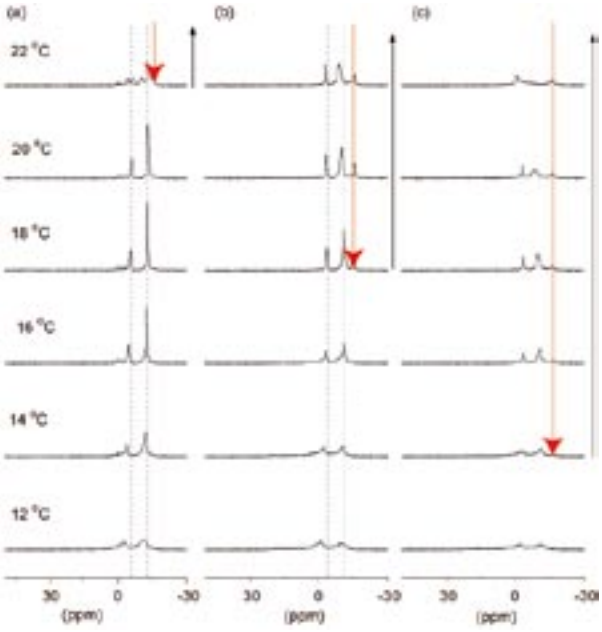

Figure 2. ^{31}P-NMR spectra of magnetically aligned bicelle prepared from (a) PIP_2/POPC/DMPC/PIP_2/DHPC, (b) POPC/DMPC/PIP_2/DHPC and (c) SAPC/POPC/DMPC/PIP_2/DHPC, respectively. The red arrows indicate $\delta_{\perp}$ edges of axially symmetric powder pattern spectra of ^{31}P chemical shift anisotropy due to the formation of MLVs. Thus black arrows indicate the temperature range of the samples containing mixture of bicelle and MLVs.

2. Solid-State ^{95}Mo NMR of Polyoxomolybdates (V, VI) with ε-Keggin Structure

For molybdenum with the oxidation number of Mo^0–Mo^{VI}, solution-state ^{95}Mo NMR has accessed all of integer oxidation number so far. In particular, ^{95}Mo NMR of Mo^0, Mo^{II} and Mo^{VI} has been widely used for study in the field of coordination chemistry and reactivity. On the contrary, investigation of solid-state ^{95}Mo NMR have been limited, because the spectra are broadened owing to the second-order quadrupole interaction. Recently, we have reported solid-state ^{95}Mo NMR of Mo^V species for the first time by measuring high-field ^{95}Mo NMR of mixed-valence polyoxomolybdates(V, VI) with localized or delocalized d^1 electrons. It has been shown that the chemical shift of ^{95}Mo NMR of Mo^V species exhibits a larger value than that of Mo^{VI}, and anisotropy of chemical shift depends on localization of d^1 electrons.

In this work, we investigated molecular and electron structures by solid-state ^{95}Mo and DFT calculation for a polyoxomolybdate crystal of $[PMo_{12}O_{36}(OH)_4\{La(H_2O)_{2.75}Cl_{1.25}\}_4]27H_2O$ (abbreviated as $\{Mo_{12}(La)\}$), where a $\{Mo_{12}\}$ core with the ε-Keggin structure is capped with four $La(H_2O)_{2.75}Cl_{1.25}$. Decimal fraction appears because of a disorder structure of H_2O and Cl coordinated to La^{III}. While potentiometric titration experiments have suggested that molybdenum is also disordered, only single Mo site was reported from analysis of X-ray diffraction. As shown in Figure 3, ^{95}Mo static NMR spectra of $\{Mo_{12}(La)\}$ were measured under moderate (9.4 T) and ultrahigh magnetic fields (21.8 T). By simulation of the NMR spectra and density functional theory (DFT) calculation for isolated anions, NMR parameters for two molybdenum sites within the crystals were obtained. It was found that the d^1 electrons in $\{Mo_{12}(La)\}$ are localized and used to form four Mo^V–Mo^V bonds.

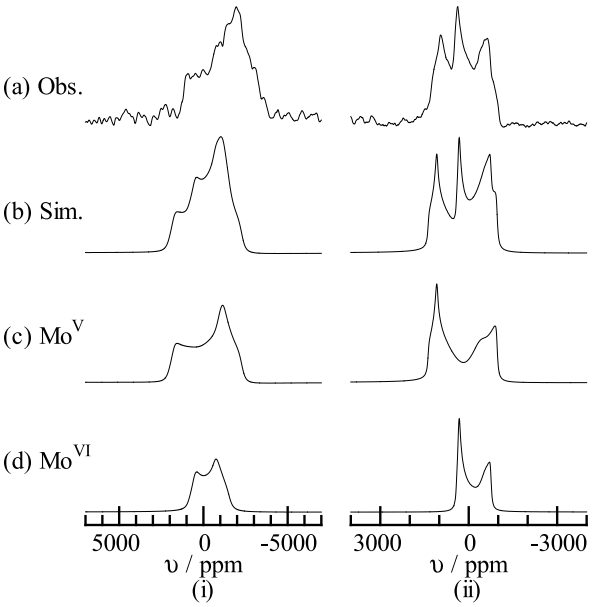

Figure 3. ^{95}Mo NMR spectra of $[\varepsilon\text{-}PMo_{12}O_{36}(OH)_4\{La(H_2O)_{2.75}Cl_{1.25}\}_4]27H_2O$ under (i) 9.4 and (ii) 21.8 T. (a) and (b) show the observed and simulated spectra, respectively. (c) and (d) denote spectral components consisting of the spectrum (b).

Organic Solar Cells

Research Center for Molecular Scale Nanoscience
Division of Molecular Nanoscience

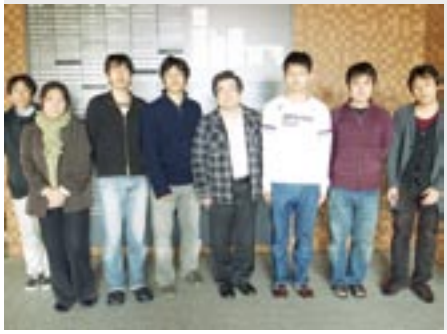

HIRAMOTO, Masahiro	Professor
KAJI, Toshihiko	Assistant Professor
IKETAKI, Kai	IMS Fellow
NAKAO, Satoru	Post-Doctoral Fellow
SHINMURA, Yusuke	Research Fellow
KUBO, Masayuki	Research Fellow
YOKOYAMA, Kazuya	Research Fellow
ISHIYAMA, Norihiro	Graduate Student
ANNEN, Sayuri	Secretary
MIYAWAKI, Makiko	Secretary

Organic solar cell is recognized as a future 3rd generation solar cell. Last year, we started CREST Project; "Bandgap Science for Organic Solar Cells." Target of this project is 15% efficiency of organic solar cells by establishing bandgap science for organic semiconductors, which is equivalent to that for silicon semiconductor.

1. Carrier Concentration Determination for Organic Semiconductors by AC Hall Effect

We accomplished the world record conversion efficiency of 5.3% by using seven-nines (7N, 0.1 ppm, 99.99999%) purified fullerene.[1,2] Taking this result into consideration, determination technique of ppm-level concentrations of impurities in organic semiconductors is very important.

Hall effect measurement is well established for inorganic semiconductors. However, for high resistant organic semiconductors, reproducible results of Hall voltage of the order of μV has not been reported. In this study, we applied the AC Hall effect technique to metal-free phthalocyanine (H_2Pc) film and succeeded to obtain the first reproducible results.

H_2Pc was purified by single-crystal formed sublimation 3 times (Figure 1). The van der Pauw type Au electrodes were formed on the 1 μm-thick H_2Pc film (Figure 2). AC Hall measurement system (Toyo Technica, Resitest 8300) was used. AC magnetic field (0.1 Hz, 0.3 T at max.) was applied perpendicular to the film surface and Hall voltage of about 10^{-6} V was precisely detected by the lock-in technique.

Carrier type was determined to p-type. Values of carrier concentration and hole mobility were determined to 3.5×10^{14} /cm^3 and 0.03 cm^2/Vs, respectively. Very small value of carrier concentration of 10^{14} /cm^3 suggests that the purity of H_2Pc film is seven nines (7N) at least.

Purification and doping technique are crucially important to realize 15% efficient organic solar cells. The present AC Hall measurement is revealed to be a powerful tool to evaluate the purity and doping concentration in organic semiconductor films.

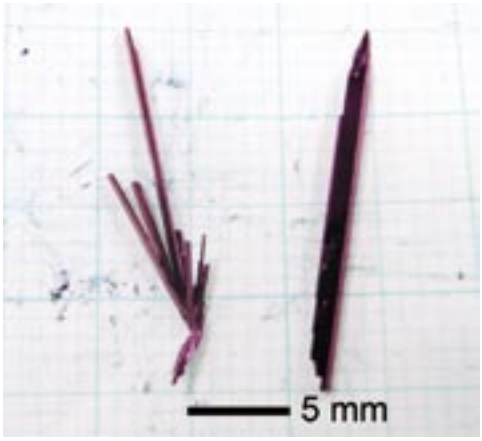

Figure 1. Photograph of single crystals of H_2Pc.

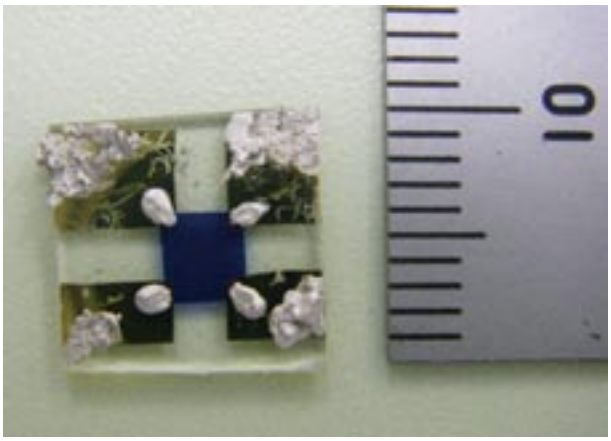

Figure 2. Photograph of H_2Pc cell for AC Hall effect measurements. Blue square part is H_2Pc film (1 μm).

2. n-Type C_{60} Formation by H_2-Doping

Hydrogen (H_2) doping effect[3] for C_{60} was investigated. Highly purified 7N-C_{60} (seven nines; 99.99999%) sample was used. Doping was performed by introducing H_2 gas (1×10^{-4} Torr) into the evaporation chamber during the co-evaporation of C_{60} and H_2Pc (Figure 3). For ITO/H_2Pc:C_{60} codeposited layer/Al cell (Figure 3), open-circuit photovoltage (V_{oc}) and short-circuit photocurrent (J_{sc}) increased from 0.3 to 0.5 V and from 2 to 5 mA/cm^2, respectively, by H_2-doping (Figure 4). Internal quantum efficiency of J_{sc} increased 4 times from 5% to 20% in the absorption region of C_{60} (400–500 nm). Similar result was observed for ITO/C_{60} single layer/Al cell.

Above results can be reasonably explained by the increase of the built-in potential, which is caused by the negative shift of Fermi level (E_F) of C_{60} by H_2-doping (Figure 5). We think that the n-type C_{60} was formed by the intentional H_2-doping. This is a clear demonstration of pn-control by the doping technique for organic semiconductors. Quantitative evaluation of donor concentration by H_2-doping is now in progress by the AC Hall effect.

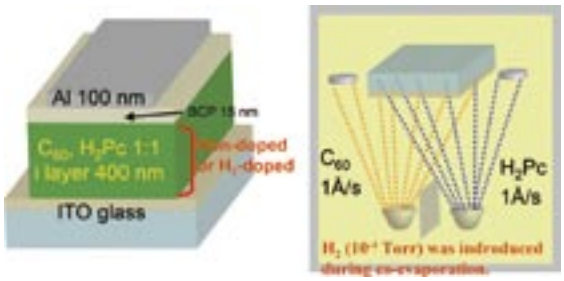

Figure 3. Sandwich-type cell of C_{60}:H_2Pc codeposited layer and H_2-doping during co-evaporation.

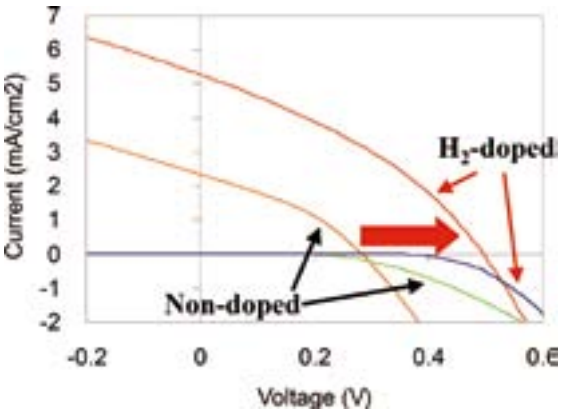

Figure 4. Current-voltage characteristics for undoped and H_2-doped cells.

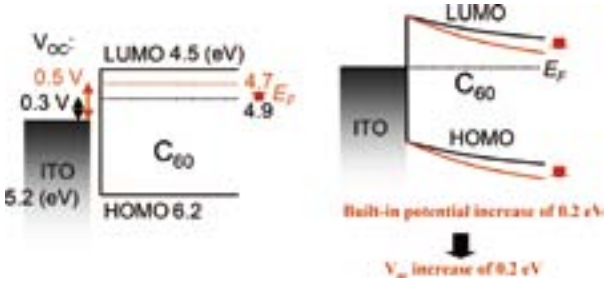

Figure 5. (a) Negative shift of Fermi level (E_F) of C_{60} by H_2-doping. (b) Increase of built-in potential caused by V_{oc} increase.

References

1) M. Hiramoto, *Proceedings of SPIE Vol. 7052, Organic photovoltaics IX*, pp 70520H-1-6, San Diego, CA, 12-14 Aug. (2008).
2) K. Sakai and M. Hiramoto, *Mol. Cryst. Liq. Cryst.* **491**, 284–289 (2008).
3) M. Hiramoto *et al.*, *Chem. Lett.* 119 (1990).

Development of Organic Semiconductors for Molecular Thin-Film Devices

Research Center for Molecular Scale Nanoscience
Division of Molecular Nanoscience

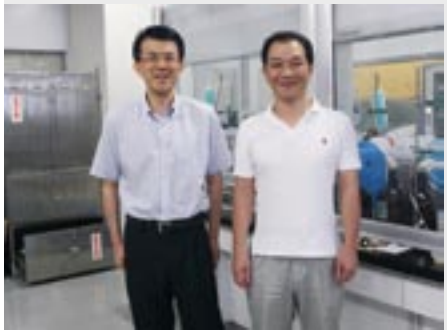

SUZUKI, Toshiyasu — Associate Professor
SAKAMOTO, Youichi — Assistant Professor
WATANABE, Yoko — Secretary

Organic light-emitting diodes (OLEDs) and organic field-effect transistors (OFETs) based on π-conjugated oligomers have been extensively studied as molecular thin-film devices. Organic semiconductors with low injection barriers and high mobilities are required for highly efficient OLEDs and OFETs. Radical cations or anions of an organic semiconductor have to be generated easily at the interface with an electrode (or a dielectric), and holes or electrons must move fast in the semiconducting layer. Compared with organic p-type semiconductors, organic n-type semiconductors for practical use are few and rather difficult to develop. Recently, we found that perfluorinated aromatic compounds are efficient n-type semiconductors for OLEDs and OFETs.

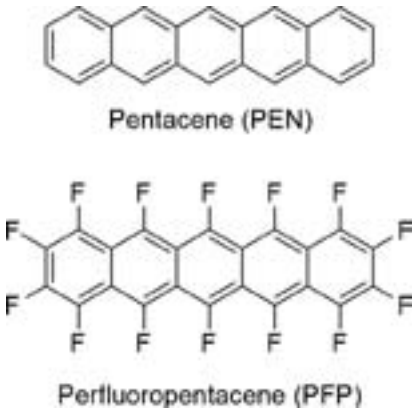

Figure 1. Molecular structures of pentacene (PEN) and perfluoropentacene (PFP).

1. Effect of Fluorination on the Molecular Packing of Perfluoropentacene and Pentacene Ultrathin Films on Ag (111)[1)]

The growth of perfluoropentacene (PFP) and pentacene (PEN) ultrathin films on Ag(111) has been investigated using low-temperature scanning tunneling microscopy. To understand the influence that perfluorination of the parent molecule has on its resultant packing structure, the results are compared against each other in the framework of morphological differences. Perfluorination leads to a different packing structure in the first monolayer. We observed only one closely packed arrangement with periodic dislocation lines for PFP molecules, while for PEN molecules, there are two coexisting arrangements in the first monolayer. Monolayers of each molecule are commensurate with the underlying substrate with long axes of both molecules aligned in the [110] direction along the silver surface. The disparity in arrangements is attributed to the difference in peripheral atoms of the two molecules. Additional photoemission spectroscopy studies reveal that PFP physisorbs on Ag (111).

2. Synthesis, Structure, and Property of Fluorinated Rubrenes

Rubrene is the tetraphenyl-substituted tetracene and has a nonplanar structure unlike pentacene. The single-crystal field-effect transistors (FETs) with rubrene have shown the highest hole mobilities up to 40 $cm^2V^{-1}s^{-1}$. We synthesized partially and fully fluorinated rubrenes for single-crystal FETs with high electron mobilities. Tetradecafluororubrene (**F14-RB**) and perfluororubrene (**PF-RB**) are red crystalline solids similar to rubrene. The electrochemical measurements showed that the first reduction potentials shifted positively in the order of rubrene, **F14-RB**, and **PF-RB** (–2.06, –1.48, and –0.92 V *vs* Fc/Fc^+, respectively). The single-crystal X-ray analyses indicated that **F14-RB** adopted the 2-D π-stacking interactions with face-to-face distances as short as 3.54 Å. In the case of **PF-RB**, no face-to-face interactions were found probably because the fluorine atoms resulted in larger molecular distances compared to the hydrogen atoms. The thin-film tran-

sistors (TFTs) with **F14-RB** and **PF-RB** have been fabricated, and they showed the n-type behaviors with the mobilities of 10^{-6} to 10^{-5} $cm^2V^{-1}s^{-1}$. These values are similar to that of the rubrene TFT. The fabrications of the single-crystal transistors are underway.

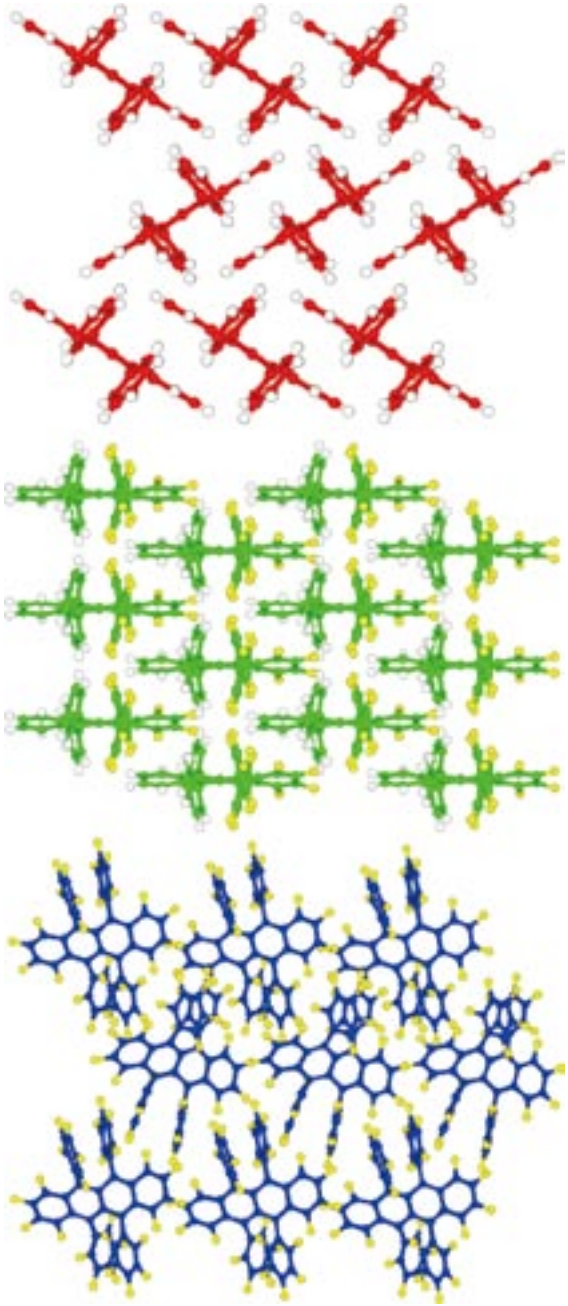

Figure 2. Crystal structures of rubrene (top), **F14-RB** (middle), and **PF-RB** (bottom).

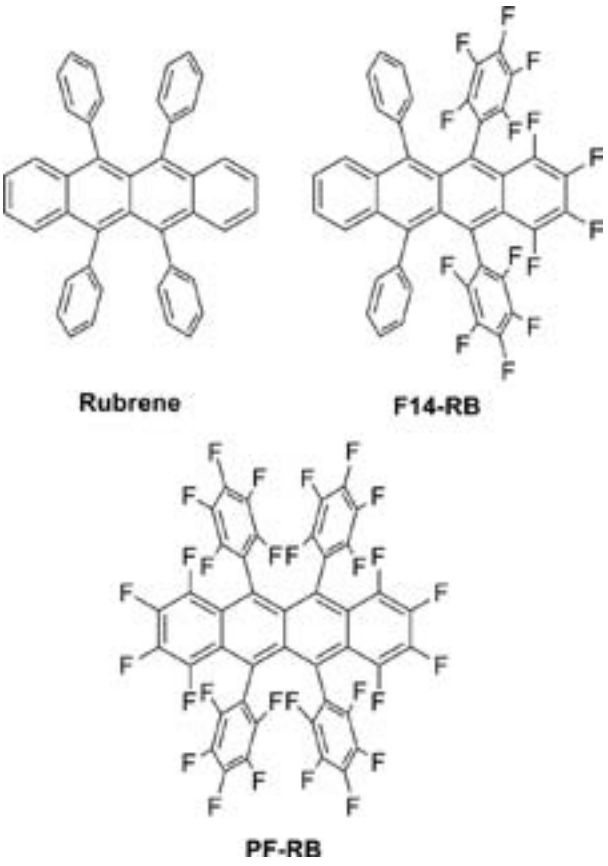

Figure 3. Molecular Structures of rubrene (top), **F14-RB** (middle), and **PF-RB** (bottom).

Reference

1) S. L. Wong, H. Huang, Y. L. Huang, Y. Z. Wang, X. Y. Gao, T. Suzuki, W. Chen and A. T. S. Wee, *J. Phys. Chem. C* **114**, 9356–9361 (2010).

Building Photosynthesis by Artificial Molecules

Research Center for Molecular Scale Nanoscience
Division of Molecular Nanoscience

NAGATA, Toshi	Associate Professor
KAWAO, Masahiro	IMS Fellow
KON, Hiroki	Post-Doctoral Fellow
MIURA, Takahiro	Graduate Student
YUSA, Masaaki	Graduate Student
WANATABE, Yoko	Secretary

The purpose of this project is to build nanomolecular machinery for photosynthesis by use of artificial molecules. The world's most successful molecular machinery for photosynthesis is that of green plants—the two photosystems and related protein complexes. These are composed almost exclusively from organic molecules, plus a small amount of metal elements playing important roles. Inspired by these natural systems, we are trying to build up multimolecular systems that are capable of light-to-chemical energy conversion. At present, our interest is mainly focused on constructing necessary molecular parts.

1. Synthesis of Single-Molecular Quinone Pools with Internal Redox Gradients and ^{19}F-NMR Handles

Mimicking photosynthesis by artificial molecules is an interesting research subject from both academic and industrial viewpoints. Although many aspects of natural photosynthesis have been successfully modeled by use of artificial molecules, there are still many important features that are yet unexplored by model chemists. One of such disregarded features is the quinone pool, which consists of a collection of quinones embedded in some biomembranes.

Previously we reported our research on building "single-molecular" quinone pools by use of synthetic dendrimer molecules.[1,2] In these molecules, the quinones were converted to quinols by irradiation of the attached porphyrin with visible light in the presence of reducing agents (thiols). However, all quinones in these molecules were the same, so that there was no chance to realize vectorial electron transport which is essential for photochemical energy conversion.

In this work, we prepared new quinone pool molecules that contained two different quinones with different redox potentials. By changing the locations of the quinones, we can control the vectorial electron transport within the pool. We also introduced fluorine atoms to the quinones, which enable selective observation of the changes in the quinone moieties by ^{19}F NMR spectroscopy.

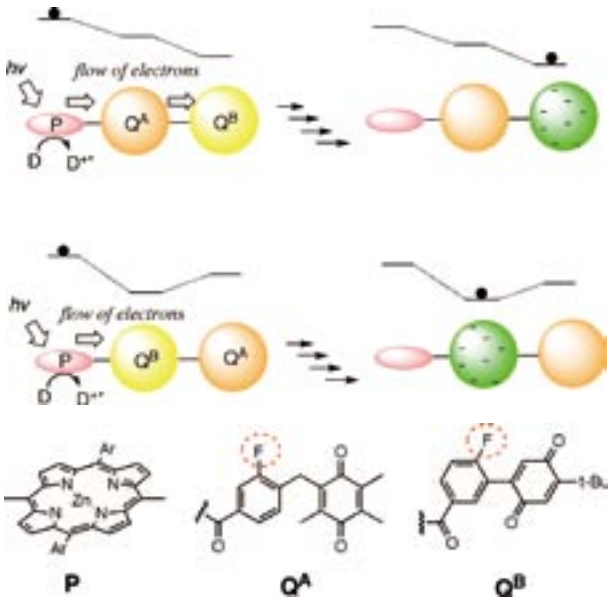

Figure 1. Pictorial representation of the quinone pool molecules in this work. P: Pigment (porphyrin), Q^A and Q^B: Quinones, D: Electron donor.

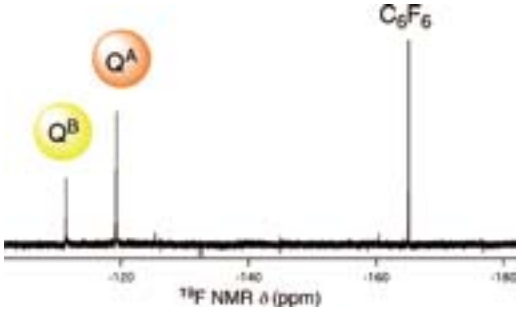

Figure 2. The ^{19}F NMR of the synthesized quinone-pool molecule.

2. Synthesis of Zinc Porphyrin/Co(II) Polypyridine Dyad Molecules by Use of Terpyridine-Bipyridine Binary Ligands

Combination of photoinduced electron transfer and redox chemistry of transition metal complexes is an attractive way to achieve useful photochemical energy and materials conversion. A number of successful systems have been reported in the literature, however most of them share one potentially disturbing issue: Use of precious metals such as Ru, Rh and Re. In addition to their high cost, they may suffer from availability problems due to the low abundance of these elements. Therefore, it is desirable to substitute them with more common elements.

In the present study, we chose Zn porphyrins as photosensitizers, and a Co(II) polypyridine complex as a redox-active metal center. The redox chemistry of Co(II) is particularly interesting, because it can be converted to a super-nucleophilic Co(I) species by one-electron reduction, which can be easily achieved by photoinduced electron transfer.

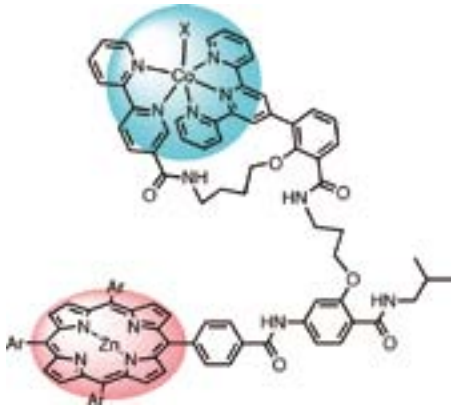

Figure 3. The Zn porphyrin/Co(II) complex dyad molecules.

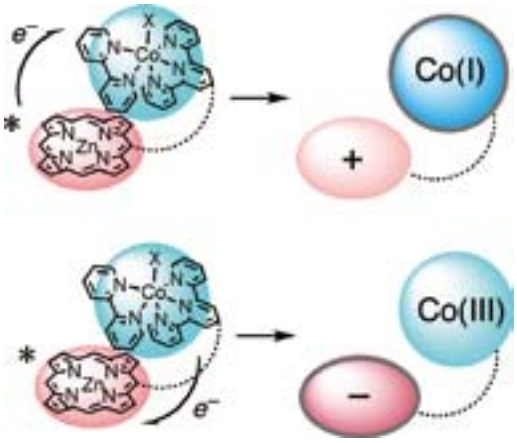

Figure 4. Two different routes for photoinduced electron transfer between the porphyrin and Co(II) complex

We synthesized a series of Zn porphyrin/Co(II) complex dyad molecules with two objectives. One is to utilize our terpyridine-bipyridine binary ligand which enabled predictable formation of Co(II) mononuclear complexes without complication by ligand exchange.[3] The other is to examine the photochemical interaction between the Zn porphyrin and the Co(II) complex in the intramolecular manner, particularly with porphyrins having various redox potentials.

3. Synthesis of Diporphyrin Molecules with Tweezer-Like Bridges

Molecules capable of dynamic conformational change are gaining interest as components of "molecular machines." Such conformational changes should be also useful in chemical energy conversions, as known in the molecular mechanism of cytochrome bc1 enzyme. Based on this consideration, we have started research on tweezer-like molecules whose photochemistry and redox chemistry can be modulated by conformational changes.

In this study, we synthesized a diporphyrin molecule with a tweezer-like bridge, where one leg of the tweezer has a zinc porphyrin and a positive charge, and the other leg has a free-base porphyrin and a negative charge. The conformation of the molecule was estimated by the intramolecular energy transfer from the zinc porphyrin to the free-base porphyrin. The conformational change in the solution phase was recorded by systematic change of the polarity and ionic strength of the surrounding media.

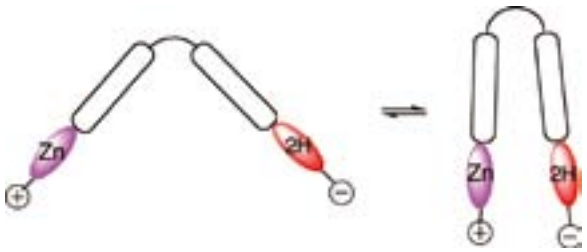

Figure 5. The dirporphyrin tweezer and the conformational change.

References

1) T. Nagata and Y. Kikuzawa, *Biochim. Biophys. Acta* **1767**, 648–652 (2007).
2) T. Nagata, Y. Kikuzawa, T. Nagasawa and S. I. Allakhverdiev, *Trans. Mater. Res. Soc. Jpn.* **34**, 505–508 (2009).
3) H. Kon and T. Nagata, *Inorg. Chem.* **48**, 8593–8602 (2009).

Chemistry of Bowl-Shaped Aromatic Compounds and Metal Nanocluster Catalysts

Research Center for Molecular Scale Nanoscience
Division of Molecular Nanoscience

SAKURAI, Hidehiro	Associate Professor
HIGASHIBAYASHI, Shuhei	Assistant Professor
TSURUOKA, Ryoji	IMS Fellow
SAL PRIMA, Yudha S.	Visiting Scientist; JSPS Invited Fellow
SCHMIDT, Bernd	Visiting Scientist; JSPS Invited Fellow
MURUGADOSS, Arumugam	Visiting Scientist; JSPS Post-Doctoral Fellow
TAN, Qi-Tao	Visiting Scientist; JSPS Post-Doctoral Fellow
VARIPARAMBIL, Sajisha Sanjayan	Post-Doctoral Fellow
JEBAMALAI, W. J. B.	Post-Doctoral Fellow
BAIG, Nasir R.	Post-Doctoral Fellow
KITAHARA, Hiroaki	Post-Doctoral Fellow/Graduate Student
TOPOLINSKI, Berit	Visiting Scientist
CHEN, Hsiao Wei	Visiting Scientist
LORPITTHAYA, Rujee	Visiting Scientist
PURUSHOTHAM, Uppula	Visiting Scientist
ANH, Dang Thi Tuyet	Visiting Scientist
KARUEHANON, Weeranuch	Visiting Scientist
KATRUN, Praewpan	Visiting Scientist
DEIVASIGAMANI, Umadevi	Visiting Scientist
REZA, A. F. G. Masud	Graduate Student
ONOGI, Satoru	Graduate Student
DHITAL, Raghu Nath	Graduate Student
KATAOKA, Keita	Graduate Student
PREEDASURIYACHAI, Patcharee	Graduate Student*
NAKANO, Sachiko	Technical Fellow
KAI, Noriko	Technical Fellow
ISHIDA, Yuka	Technical Fellow
KIM, Yukimi	Technical Fellow
SASAKI, Tokiyo	Secretary
YURIKUSA, Tomoko	Secretary
TANIWAKE, Mayuko	Secretary

Bowl-shaped π-conjugated compounds including partial structures of the fullerenes, which are called “buckybowls,” are of importance not only as model compounds of fullerenes but also as their own chemical and physical properties. Heteroatom-containing buckybowls (heterobuckybowls) have also been expected to exhibit unique physical characters. For example, in solution they show the characteristic dynamic behavior such as bowl-to-bowl inversion. On the other hand, they sometimes favor stacking structure in a concave-convex fashion in the solid state, giving excellent electron conductivity. Furthermore, some buckybowls are conceivable to possess the bowl-chirality if the racemization process, as equal as bowl-to-bowl inversion, is slow enough to be isolated. However, very few buckybowls/heterobuckybowls has been achieved for preparation mainly due to their strained structure, and no report on the preparation of chiralbowls has appeared. In the present project, we develop the rational route to the various kinds of buckybowls/heterobuckybowls with perfect chirality control using the organic synthesis approach.

We also investigate to develop novel catalytic properties of metal nanoclusters. We focus on the following projects: Preparation of size-selective gold nanoclusters supported by hydrophilic polymers and its application to aerobic oxidation catalysts: Synthetic application using metal nanocluster catalyst: Development of designer metal nanocluster catalyst using the highly- functionalized protective polymers.

1. Optical Resolution of Chiral Buckybowls by Chiral HPLC[1)]

Buckybowls have been a focus of recent attention because of their interesting physical properties derived from the bowl-shaped π-conjugated aromatic structure. One of the interesting features of the structure is the chirality of these spherical aromatic compounds unlike planer ones, named *Bowl chirality*. The bowl chirality is expected to provide fascinating characters for their applicability not only for asymmetric molecular recognition and chiral ligands for transition metals, but also for precursors of chiral fullerenes and carbon nanotubes in chemical synthesis. Enantiopure or -enriched chiral buckybowls could be obtained by either asymmetric synthesis or optical resolution of racemate. As an example of the former, we have recently achieved the first enantioselective synthesis of chiral trimethylsumanene (**1**) (Figure 1) by converting chirality based on sp^3 carbon to bowl chirality. In contrast, the latter approach has not been reported, although those of related chiral fullerenes and carbon nanotubes have been reported. We focus on optical resolution of chiral buckybowls, trimethyltris-(trimethylsilyl)sumanene (**2**) and trimethylsumanenetrione (**3**) (Figure 1), by chiral HPLC, and determination of bowl inversion energy barrier of **3** by CD spectra.

Optical resolution of racemic trimethyltris(trimethylsilyl) sumanene (**2**) was initially investigated for the following reasons. The ee of enantioselectively prepared substituted sumanenes would be easily determined by the chiral HPLC analysis of the tris(trimethylsilyl)-derivatives as well. Chiral column DAICEL CHIRALPAK® IA, which is composed of

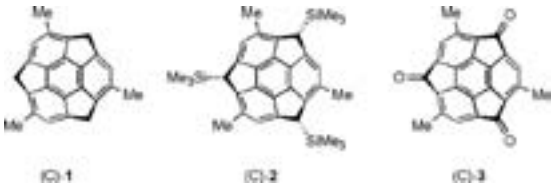

Figure 1. Structures of (*C*)-8,13,18-trimethylsumanene (**1**), (*C*)-(8*R*,13*R*,18*R*)-10,15,20-trimethyl-8,13,18-tris(trimethylsilyl)sumanene (**2**), and (*C*)-10,15,20-trimethylsumanene-8,13,18-trione (**3**).

amylose tris(3,5-dimethylphenylcarbamate), realized the desired optical resolution.

Next, we investigated the optical resolution of racemic **3**. The racemization energy barrier of **3** was estimated to be ca. 23.5 kcal/mol, which corresponds to ca. 44 h half-life at 10 °C. This could be sufficiently high to obtain enantioenriched **3** in HPLC time-scale. Racemic **3** was prepared by aerobic oxidation of racemic **1** (Scheme 1). Reaction of **1** with sodium hexamethyldisilazide and molecular oxygen in DMF at low temperature for 5 min gave the desired product in 26% yield. As expected, optical resolution of **3** was attained at 9 °C and afforded each enantioenriched sample of **3**. Absolute configuration of each enantiomer was assigned as (*A*)-**3** (t^R = 17 min) and (*C*)-**3** (t^R = 18 min) by the fact that enantioenriched sample prepared from (*C*)-**1** possessed t^R = 18 min.

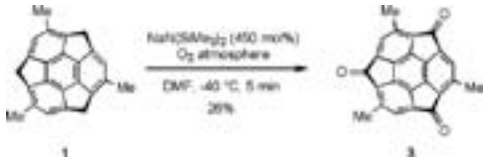

Scheme 1. Synthesis of trimethylsumanenetrione (**3**).

With enantioenriched **3** in hand by chiral HPLC separation, the bowl inversion energy barrier of **3** can be determined by CD spectra measurement. Bowl inversion is a characteristic feature of buckybowls and has been extensively studied by experimental and theoretical methods. A limitation of commonly used NMR methods for experimental determination of the energies is that those of buckybowls without diastereotopic protons cannot be determined by the technique. In contrast, the energies of enantiopure or -enriched chiral buckybowls even without diastereotopic protons such as **3** can be determined by CD spectra measurement because they are racemized though bowl inversion. By time-dependent decay of the intensity of CD spectra of **3** at 255 nm at 30 °C (Figure 2), the energy barrier was determined to be 23.4 and 23.3 kcal/mol in CH_3CN and CH_2Cl_2, respectively. These experimental values showed good agreement with predicted values.

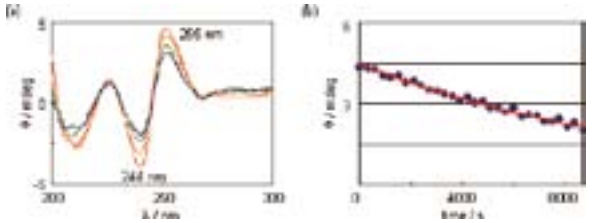

Figure 2. (a) Time-dependent decay of intensity of CD spectra of (*A*)-**3** in CH_3CN at 30 °C (red: 0 h, orange: 1 h, green: 2 h, blue: 3 h). (b) Decay of ellipse θ and their fitting curve at 255 nm in CH_3CN at 30 °C.

2. Stereoselective Cyclotrimerization of Enantiopure Iodonorbornenes Catalyzed by Pd Nanoclusters for C_3 Symmetric *syn*-Tris(norborneno)benzenes[2)]

C_3 or C_{3v} symmetric enantiopure *syn*-tris(norborneno) benzenes with various functional groups were synthesized through Pd-catalyzed cyclotrimerization of enantiopure iodo norbornenes. The generality of Pd-catalyzed cyclotrimerization for *syn*-tris(norborneno)benzenes were well-demonstrated.

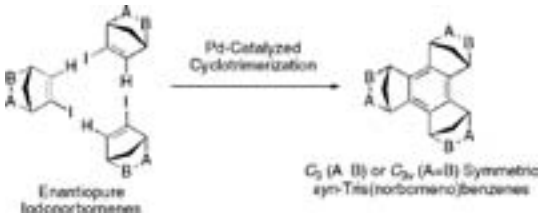

Scheme 2. Pd-catalyzed cyclotrimerization of iodonorbornenes.

3. Gold Nanocluster as a Catalyst for Intramolecular Addition of Primary Amines to Unactivated Alkenes under Aerobic Conditions[3)]

Gold nanoclusters stabilized by hydrophilic polymer, poly(*N*-vinyl-2-pyrrolidone) (Au:PVP), catalyzed the intramolecular addition of primary amines to unactivated alkenes in good yield in the presence of formic acid derivatives under aerobic conditions. Since Au:PVP also promotes the cycloaddition of toluenesulfonamides under basic conditions, Au:PVP catalyst is expected to be a versatile and easy-to-handle catalyst for hydroamination reactions.

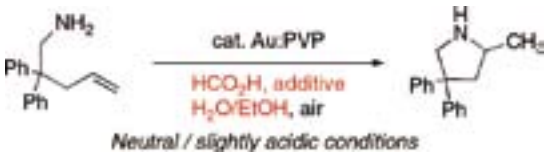

Scheme 3. Au:PVP-catalyzed Hydroamination.

References

1) R. Tsuruoka, S. Higashibayashi, T. Ishikawa, S. Toyota and H. Sakurai, *Chem. Lett.* **39**, 646–647 (2010).

2) S. Higashibayashi, A. F. G. Masud Reza and H. Sakurai, *J. Org. Chem.* **75**, 4626–4628 (2010).

3) H. Kitahara and H. Sakurai, *Chem. Lett.* **39**, 46–48 (2010).

Award

HIGASHIBAYASHI, Shuhei; The 24th Young Scholar Lectures in the 90th Annual Meeting of CSJ.

* carrying out graduate research on Cooperative Education Program of IMS with Chulalongkorn University

Multifunction Integrated Macromolecules for Molecular-Scale Electronics

Research Center for Molecular Scale Nanoscience
Division of Molecular Nanoscience

TANAKA, Shoji Assistant Professor

Single molecular science and technology are the new frontier for physical and synthetic organic chemistry. Especially quantum device engineering is a promising field. Recently the power consumption of information processing systems becomes critical issues, and the growing demand for ultra-low-power device has led to a greater interest in a single electron tunneling (SET) device. A SET device manipulates an electron by means of one-by-one electron transfer, resulting in ultimately low power consumption. However, for room temperature operation, the size of SET device must be as small as a few nm to overcome the thermal fluctuation problems. The process size of a few nm is out of the range of conventional micro-technology, and therefore new nano fabrication approaches for SET device have been explored worldwide.

In this project, to establish an innovative fabrication process for SET device systems, we have been developing step-wise synthetic protocols for integrating molecule-based quantum device elements (quantum dots, wells, and tunnel junctions) within a single planar macromolecule. Our strategy is based on "modular architecture" using a library of basic functional building blocks, and so far we have developed various types and sizes of 1-dimensional (1D) building blocks (**1-3**). Now we shift to the next stage, that is, the development of multi-terminal building blocks for the step-wise fabrication of planar 2-dimensional (2D) macromolecular systems.

1. Development of Multi-Terminal Molecular Building Blocks for Precisely Defined Functional 2D-Macromolecules

To synthesize a precisely defined 2D-macromolecule we first prepared three types of multi-terminal modules (**4-20**). Figure 1 shows the molecular structures. The module Type-1 is a conductive junction block, in which the π-system of the main chain and that of the side chain are fully conjugated. The type-2 is a multi-terminal tunnel/capacitive junction block: The main chain and the side chain are electronically coupled by tunnel or capacitive junction. The type-3 is an insulating spacer block: The side chain is used to prevent electrical short circuits between the conductive parts and to maintain a desired structure of the 2D system. Now we are challenging to fabricate planar 2D macromolecules operating as an individual SET device from these trial modules.

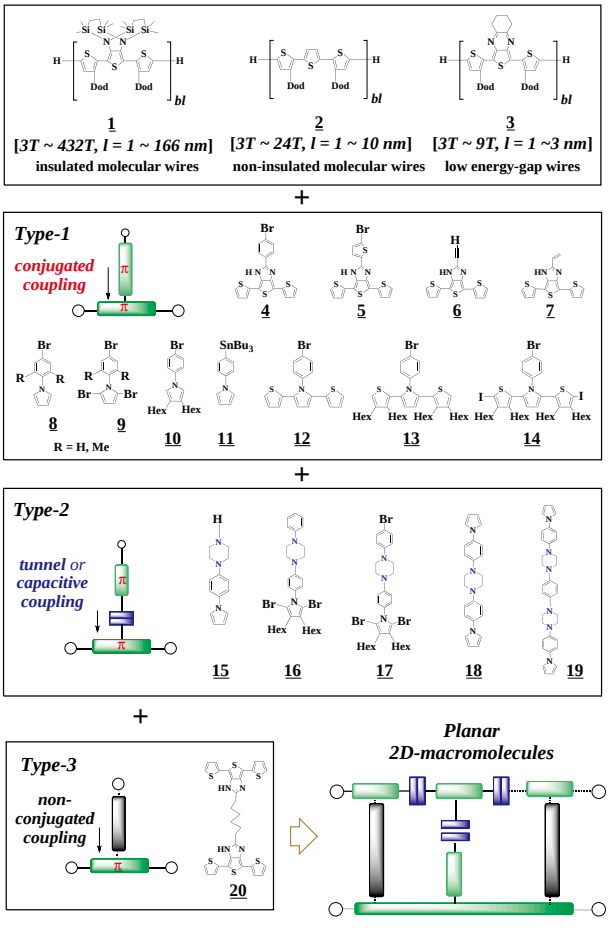

Figure 1. Structures of wire and multi-terminal modules.

Development of Novel Heterocyclic Compounds and Their Molecular Assemblies for Advanced Materials

Safety Office

TOMURA, Masaaki Assistant Professor

Heterocycles containing sulfur and/or nitrogen atoms are useful as components of functional organic materials since heteroatoms in their rings are helpful to stabilize ions or ion-radical species. In addition, intermolecular interactions caused by heteroatom contacts can be expected to form unique molecular assemblies. In this project, novel functional organic materials based on various heterocycles were synthesized and their physical and structural properties were investigated.

1. A Two-Dimensional Ladder-Type Network in the 2:1 Co-Crystal of 1,2,5-Thiadiazole-3,4-dicarboxylic Acid and 4,4'-Bipyridine[1)]

The crystal structure of the 2:1 co-crystal of 1,2,5-thiadiazole-3,4-dicarboxylic acid and 4,4'-bipyridine has been determined by X-ray diffraction. Two intramolecular O–H···N [2.730(7) Å] and O–H···O [2.433(6) Å] hydrogen bonds are observed in the thiadiazole molecule. In the crystal structure, the molecules form a unique two-dimensional ladder-type network linked by intermolecular O–H···N [2.704(4) Å] hydrogen bonds and S···O [3.100(5) Å] heteroatom interactions.

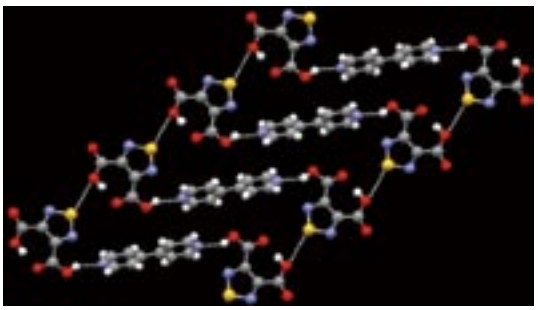

Figure 1. A unique two-dimensional ladder-type network.

2. A BF_2 Complex of a Dihydroxydione with a Perfluorotetracene Skeleton[2)]

A BF_2 complex containing an octafluorotetracene moiety was synthesized as a new type of electron acceptor. This compound exhibits a long-wavelength absorption based on the perfluorotetracene skeleton and high electron affinity due to its quadrupolar structure enhanced by fluorination. The BF_2 complex exhibited n-type semiconducting behavior.

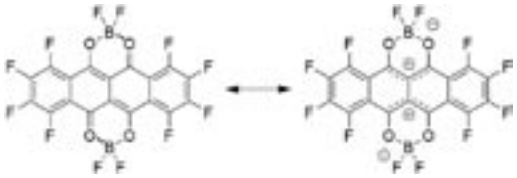

3. Photovoltaic Properties of (*E*)-2-Cyano-3-[4-(diphenylamino)phenyl]acrylic Acid Substituted by *tert*-Butyl Groups[3)]

The title dye and its related compounds were synthesized. The *tert*-butyl substituents decreased molecular stacking in the crystals, thus affecting the photovoltaic properties of the dyes. A solar cell using the dye exhibited higher performance than that for the analog without *tert*-butyl group substitution.

References

1) M. Tomura and Y. Yamashita, *Struct. Chem.* **21**, 107–111 (2010).
2) K. Ono, J. Hashizume, H. Yamaguchi, M. Tomura, J. Nishida and Y. Yamashita, *Org. Lett.* **11**, 4326–4329 (2009).
3) K. Ono, T. Yamaguchi and M. Tomura, *Chem. Lett.* **39**, 864–866 (2010).

Visiting Professors

Visiting Professor
NAKAZAWA, Yasuhiro *(from Osaka University)*

Low-Temperature Calorimetric Studies of Organic Conductors and Organic Magnets

The calorimetry system equipped with the dilution refrigerator of instrument center (Kelvinox300 Oxford Instruments) is under construction at IMS. We have prepared a Ag-based relaxation calorimetry cell which are consisting of tiny film heater and a chip type ruthenium oxide sensor. The magnetoresistance of the sensor has been measured and we have confirmed that the sensor is available up to 16 T. The heat capacity measurement of a 45 μg single crystal of κ-$BETS_2FeCl_4$ has been succeeded in a temperature range between 100 mK and 2 K. This compound is known as an organic magnetic superconductor in which superconductivity and magnetic order coexists below about 120 mK. A large thermal anomaly due to the long range ordering of Fe^{3+} has been observed at 500 mK. The application of weak magnetic fields reduces the peak temperature which is consistent with the behavior of typical antiferromagnetic system. The experiment to clarify relationship between magnetism and superconductivity is in progress now. The microchip calorimetry devices obtained by the micro-fabrication technique will be installed in the dilution refrigerator in order to study μg class single crystal samples with high resolution.

Visiting Professor
SEKIYA, Hiroshi *(from Kyushu University)*

Spectroscopic Study on Intermolecular Interactions and Dynamics in Hydrogen-Bonded Clusters and Coordination and Solvation Structures of Transition Metal Ions

We investigate the structures, intermolecular interactions, and dynamics associated with hydrogen-bonded networks in crystals as well as in the gas phase. These studies provide insights into dynamics of hydration water on the surface of proteins. Rearrangement of water networks has been observed for model hydrated amino groups in the gas phase. In molecular crystals, cooperative multiple-proton transfer along one-dimensional hydrogen-bond networks has been investigated. We also investigate the coordination and solvation structures of transition-metal ions. $Co^+(NH_3)_n$, $Ag^+(NH_3)_n$ and $Ni^+(NH_3)_n$ are studied by infrared spectroscopy and quantum chemical calculations. Ag^+ and Ni^+ adopt tetrahedral and square-planar coordination, and a distorted tetrahedral coordination, respectively. The results demonstrate a close relationship between the d-electron configurations of the metals and the geometric structures of the solvated complexes.

Visiting Professor
OHTA, Nobuhiro *(from Hokkaido University)*

Photoirradiation Effects on Magnetic Property of Organic Conductors and Ionic Conductors

Photoinduced change in the electrical conductivity of organic conductor or ionic conductor has been examined with the time-resolved measurements of the change in resistance following photoirradiation or with the impedance spectroscopy in the absence and presence of photoirradiation. In the photoirradiated organic crystals, conductivity switching and bistability of current over certain ranges of applied voltages have been observed. In organic superconductors, photoinduced change in the electrical conductivity has been also examined at temperatures in the vicinity of the metal–superconductor (M–S) phase transition temperature, and unconventional asymmetry of critical slowing down about the M–S transition temperature has been found. In ionic conductor such as silver iodide, photoirradiation effect on ionic conductivity has been observed, depending on the excitation wavelength. To understand the photoirradiation effect as well as the synergy effect of photoirradiatin and applied electric field on electrical conductivity, photoirradiation effects not only on the electrical conductivity but also on the magnetic property will be examined.